Evaluating the Crack Initiation Toughness, Crack Resistance Curves, and Tensile Properties of Two Materials in High-Pressure Hydrogen Gas

API TECHNICAL REPORT 21C

FIRST EDITION, XXXXXXXXXX 202X

Table of Contents

1 Scope

Understanding the fracture behavior of metallic materials in high pressure H2 environment can be useful for selection of materials in underground H2 storage. Currently, there is sparse data on fracture mechanics of metallic materials typically used in oil and gas well construction when subject to high pressure H2 gas environment This test program is an effort to generating data to provide some insight into testing procedures, material behavior which over time could help the industry in evaluation and selection of materials in such service.

2 Normative References

3 Term, Definitions, and Abbreviations

3.1 Terms and Definitions

3.2 Abbreviations and Variables

ε_p plastic strain

ΔK stress intensity factor range

FCGR fatigue crack growth rate

FT fracture toughness

PH precipitation hardened

RA reduction in area

RT room temperature

SCE saturated calomel electrode

SCGR static crack growth rate

SSR slow strain rate

SWCP seawater under cathodic potential

TF time to failure

UTS ultimate tensile strength

WOL wedge opening loading

4 Background

4.1 General

Achieving net-zero carbon emissions by mid-century will require a transformation of the power and energy infrastructure, including the transition to hydrogen as a fuel of the future. While it is anticipated that hydrogen in near-term will be used in primarily smaller scale applications such as portable power, public transportation vehicles, and space applications, it is foreseeable that the future use of hydrogen would include steel and cement manufacturing, industrial heat, maritime and rail applications. A hydrogen-based economy, which uses hydrogen in large industrial applications, will require an infrastructure that can deliver green hydrogen from its source to the end users. Due to the low energy density of hydrogen, large volume and a steady supply of hydrogen is required to use hydrogen in large scale industry applications. Therefore, it is expected the gas storage, transmission and delivery infrastructure will all play critical roles in a hydrogen-based economy. Currently there are ongoing efforts in the industry to understand and overcome the challenges of transporting hydrogen in the vast pipeline networks in many countries around the world. In addition to using pipeline network for hydrogen transmission, large scale storage options beyond surface storage tanks or cryogenic vessels are needed.

Geological formations such as salt caverns, depleted wells, mines, aquifers, hard rock caverns and mine seams to provide a means to store large volumes of hydrogen and thus, would have significant impact in providing the required energy in a hydrogen-based economy. The benefits and drawbacks of each of the above listed geological formations for hydrogen storage have been extensively reviewed [1-3]. However, many other critical factors, such as material properties and hydrogen-fluid interactions remain to be investigated.

While a significant amount of work has been performed in characterizing the behavior of C-Mn steels, and low alloy steels in high pressure hydrogen, significantly less information is available on the performance of high strength martensitic stainless steels in high pressure hydrogen. Alloy 718 is one of the most commonly used precipitation hardened (PH) nickel-based alloys. Prior work in literature from the early 1970's suggests that 718 is susceptible to hydrogen embrittlement [4]. Similar to steels, the fracture toughness of 718 decreases asymptotically with hydrogen pressure[4]. The fatigue crack growth rate (FCGR) values of 718 is dependent not only on ΔK, but also on the hydrogen pressure and load frequency[5]. The fracture toughness behavior of alloy 718 as a function of H_2 pressure is shown in Figure 1. The results indicate that alloy 718 can be susceptible to hydrogen embrittlement and the K_{th} decreases sharply with increasing pressure of H_2 and reaches a plateau value of about 40 – 50 MPa.$m^{1/2}$ at pressures in the range of 100 – 200 bara (see Figure 1) [4, 6]. The high susceptibility of alloy 718 is likely due to a combination of the high strength and planar deformation characteristics of the alloy.

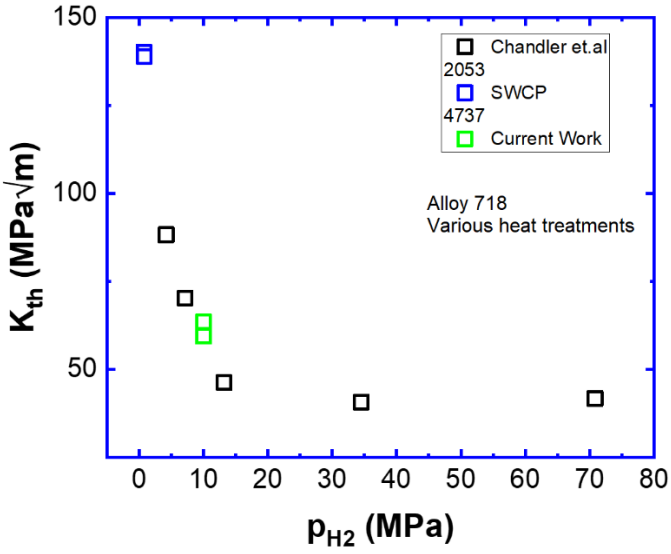

Figure 1. K_{th} vs p_{H2} for Alloy 718 at room temperature (RT)

There are significant challenges associated with accurately representing the material response over a wide range of environmental and loading conditions, to develop information needed to facilitate design. The following are several critical variables that can be considered in evaluating material properties for hydrogen storage application.

4.2 Material Effects

Higher strength grades materials in the storage wells tend to be either 4130 (UNSG414300) /4140 (UNSG41400) or 4340 steels [P110, C-110, and 8630 (UNSG86300)], which are heat treated to obtain the appropriate mechanical properties. Broadly, the fatigue crack growth rate behavior of various steels in high pressure hydrogen is not particularly sensitive to the yield strength or metallurgical condition[7]. However, the fracture toughness behavior of low alloy steels in high pressure hydrogen tends to be a strong function of the yield strength, and metallurgical condition[8, 9]. In general, fracture toughness values have been found to decrease asymptotically with increasing hydrogen pressure[10]. Typically, in high pressure hydrogen increasing yield strength has been found to lead to a decrease in the fracture toughness values[8, 9]. Chemistry, heat treatment, and microstructural design aimed at altering H trapping and/or the deformation characteristics have been shown to influence the K_{th} response in the presence of hydrogen[11, 12]. For example, vanadium (V) additions to steels are often used to form carbides that can act as irreversible traps for H and thus can improve the resistance to hydrogen embrittlement[11, 12]. However, un-tempered martensite, phosphorous (P), and sulfur (S) segregation at grain boundaries have been shown to reduce the resistance of the materials to hydrogen embrittlement[13-15].

There have been studies on austenitic stainless steels, ferritic steels, duplex alloys, and nickel-based alloys to evaluate their susceptibility to hydrogen embrittlement. Unstable austenitic alloys either due to formation of strain induced martensite or due to ordering effects can result in susceptibility to hydrogen embrittlement[16]. Alloys like SS301(UNSS30100), which are unstable due to the low nickel content and thus easy to form strain induced martensite, are more susceptible to H_2 cracking than alloys like SS310 (UNS31000) which are stable. Ferritic alloys like 29-4-2 tend to have improved resistance to hydrogen embrittlement compared to the unstable austenitic alloys in high pressure H_2, as reflected by the increase in K_{th} as well as the lower static crack growth rate (SCGR)[16, 17]. It is speculated that the high susceptibility of the unstable stainless steels is associated with the transformation of the austenite to martensite at the crack tip, coupled with the high solubility of H in the surrounding austenite matrix[16]. The reservoir of hydrogen in the austenite matrix serves to increase in the susceptibility as the austenite is transformed to martensite at the crack

tip (due to the high strains)[16, 17]. In case of the ferritic steels, the higher diffusivity of hydrogen through the matrix as well as the absence of a phase transformation is likely responsible for the improved resistance to hydrogen embrittlement[16, 17].

4.3 Loading Mode Effects

Applied K-rate has also been found to have a significant effect on the measured value of K_{th}, with K_{th} decreasing with K-rate before reaching a plateau value at low K-rates[10, 18]In lower strength materials, K_{th} increases when measured using decreasing K based approaches like wedge opening loading (WOL) or double-cantilever beam specimens[8]. It is clear from the above discussion that the effect of applied K-rate on K_{th} is a function of environmental conditions, and the deformation characteristics of the materials involved. Slow rising displacement technique has been shown to provide a lower bound value of K_{th} for materials in high pressure hydrogen[8, 19]. However, in storage applications, materials are more likely to experience a constant load with low amplitude ripples. The role of low amplitude ripples in promoting crack growth is not well understood. Hence, in addition to characterizing the minimum properties of the material using slow rising displacement methods, it is also important to understand the effect of field representative loading conditions on the K_{th} and crack growth rate performance of materials.

4.4 Environmental Effects

4.4.1 Hydrogen Pressure and Temperature

As discussed above hydrogen pressure plays a significant role on the K_{th} behavior of various materials[4, 10].

Crack growth rate and K_{th} in high pressure hydrogen environment are affected by temperature as well. The effect of temperature on the CGR for alloy 903, a high strength PH nickel alloy, is shown in reference [20]. The highest CGR and lowest K_{th} in high pressure H_2 is obtained at RT, suggesting that that the minimum fracture properties may occur at RT for these class of alloys[20]. The increase in the crack growth rate in IN903 up to 298K was attributed to the increased lattice hydrogen diffusion with increasing temperature. At higher temperatures, the increase in the K_{th} can be attributed to the effects of trapping at sheared γ', additional dislocations, leading to a decrease in mobile hydrogen concentration [6].

The above discussion suggests that the material properties in high pressure hydrogen are sensitive to hydrogen partial pressure and temperature. It is possible that the worst-case performance at a given hydrogen partial pressure can occur at intermediate temperatures and the worst performance temperature can vary with hydrogen partial pressure.

4.4.2 Impurity Effects

It is expected impurities, such as O_2, H_2O, H_2S and others may be present with hydrogen in underground storage sites. These impurities can have an impact on the material properties in high pressure gaseous hydrogen environment since some of them could competitively adsorb on metallic materials against such as O_2, and H_2O with the latter naturally present in rock formations. A small amount of oxygen could potentially act as an inhibitor to mitigate cracking of materials in gaseous hydrogen environment.

It was speculated that the presence of H_2O and H_2S are likely to increase the susceptibility of low alloy steels to embrittlement as opposed to the nominally dry H_2 conditions. However, there is no concrete evidence that supports the notion that the presence of these impurities does in fact increase the susceptibility. There is limited evidence which suggests that the presence of H_2O in the range of 30 - 40 ppm can increase the FCGR in the 5 - 10 MPa$\sqrt{m}$ ΔK regime for steels.

The role of impurities like H_2O and H_2S on the fracture behavior of the various alloys of interest has not been investigated in detail. Limited work on SS301 suggests that addition of ~3 % H_2O at 1 bara of H_2 does not significantly affect the K_{th} values both at 25°C and 75°C, though the crack growth rate decreases in the presence of H_2O [21]. The absence of an effect of H_2O on the K_{th} suggests that the critical concentration of H for crack initiation is not affected by H_2O [21]. Permeation studies on SS304 in H_2 in the presence of H_2S suggest that H_2S enables formation of sulfide cases which appear to lower the hydrogen permeation on Palladium coated samples[22]. This would suggest that the presence of H_2S in gaseous H_2 for stainless steels may not be as detrimental as pure H_2.

It is clear that there are a number of critical variables that influence the hydrogen embrittlement behavior of low alloy steels, austenitic stainless steels and nickel-based alloys in high pressure H_2. The hydrogen embrittlement response as measured via K_{th} and CGR represents a complex interaction between the environmental, loading, and microstructural variables. Hence, it is not easy to establish simple heuristics to assess hydrogen embrittlement resistance in high pressure H_2. Based on this understanding, API initiated a test program to explore the hydrogen embrittlement in high pressure H_2 of two commonly used materials (4140-125K and 718-125K) in down hole applications. The aim of the program was to understand:

a) The impact of various test methods and their parameters on the hydrogen embrittlement response in high pressure H_2 of the two materials
b) A comparison of the lab-to-lab variation in the test data for one set of material
c) Measure hydrogen permeation to estimate the solubility and permeability of H in the respective alloys.

5 Summary of Testing Program Results

5.1 General

The testing scope consisted of performing slow strain rate (SSR) tests, hydrogen permeation tests and rising displacement fracture toughness tests. All environmental tests were performed at room temperature in 100 bara H_2.

5.2 SSR Results

The SSR results for 4140 steel performed at strain rate of 1.25 X 10^{-5} s^{-1}.are summarized in Table 1. The initial target strain rate was10^{-5} s^{-1} but the actual testing strain rate ended up being bit higher. Several variables such as plastic strain (ε_p), ultimate tensile strength (UTS), reduction in area (RA) as well as the ratio of these variables in hydrogen to in nitrogen (inert) were measured from the test. As shown, except for the UTS, all other variables showed significant reduction for the samples tested in hydrogen, indicating there is an effect from the high-pressure hydrogen. The specimens tested in H_2 exhibited secondary cracking on the gage length of the specimen.

Table 1. SSR testing results for 4140-125K steel

Sample ID	Env	UTS (ksi)	UTS_{env}/UTS_{inert}	ε_p (%)	$\varepsilon_{p,\,env}/\varepsilon_{p,\,inert}$	RA (%)	$\%RA_{Env}/\%RA_{Inert}$
4738-SSR3	N_2	154		18.2		54.977	
4738-SSR7	N_2	154.9		17.4		56.106	
4738-SSR8	N_2	155.2		17.2		57.612	
4738-SSR4	H_2	149.7	0.968	7.5	0.426	13.969	0.249
4738-SSR5	H_2	153	0.989	7.8	0.443	8.24	0.147

4738-SSR6	H_2	153.8	0.994	8.4	0.477	13.877	0.247

The SEM photomicrographs of the 4140-125K steel tested in nitrogen and hydrogen are shown in Figure 2 and 3 respectively.

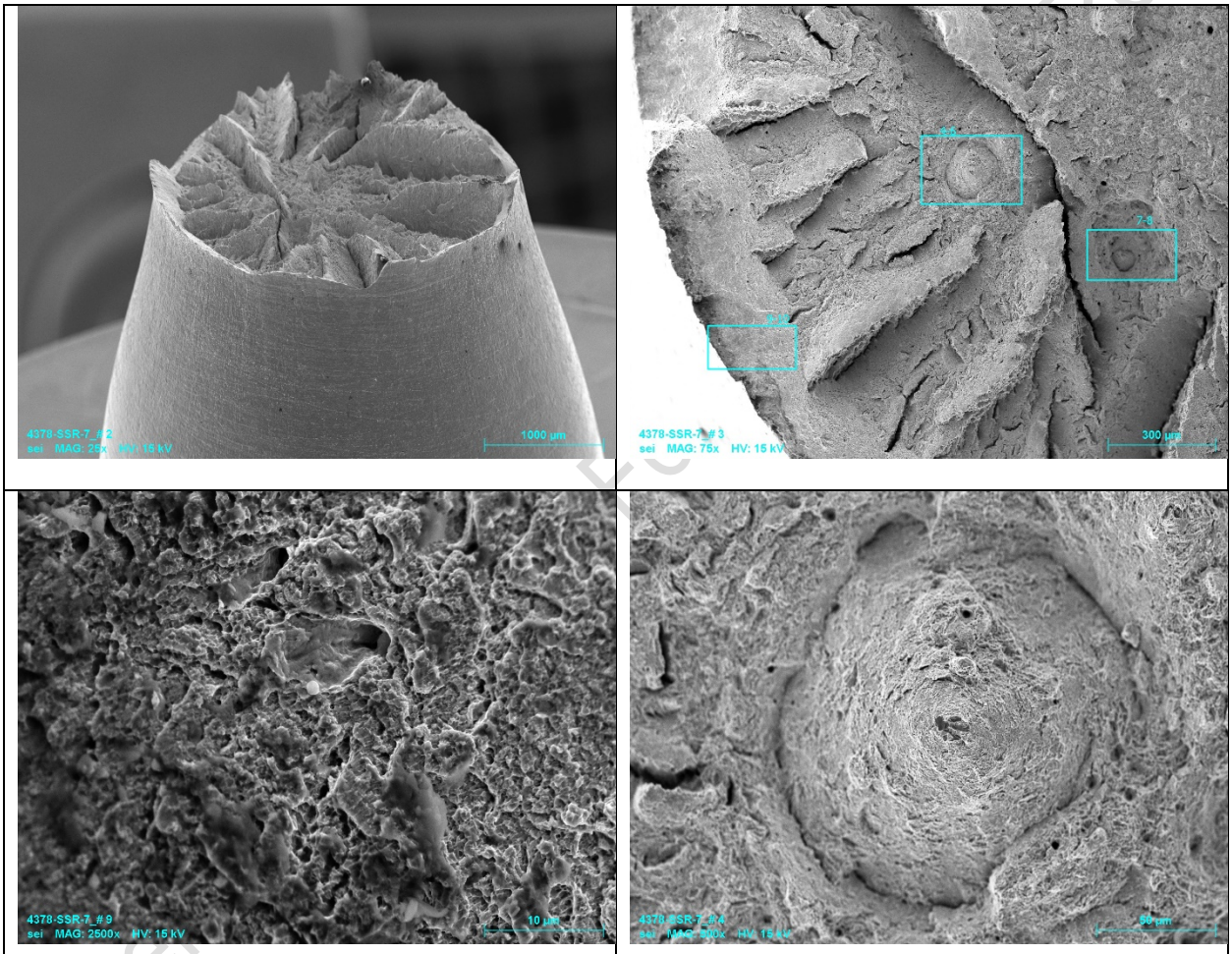

4738-SSR7, in nitrogen

Figure 2 SEM photomicrographs of the SSR sample for 4140 steel tested in nitrogen

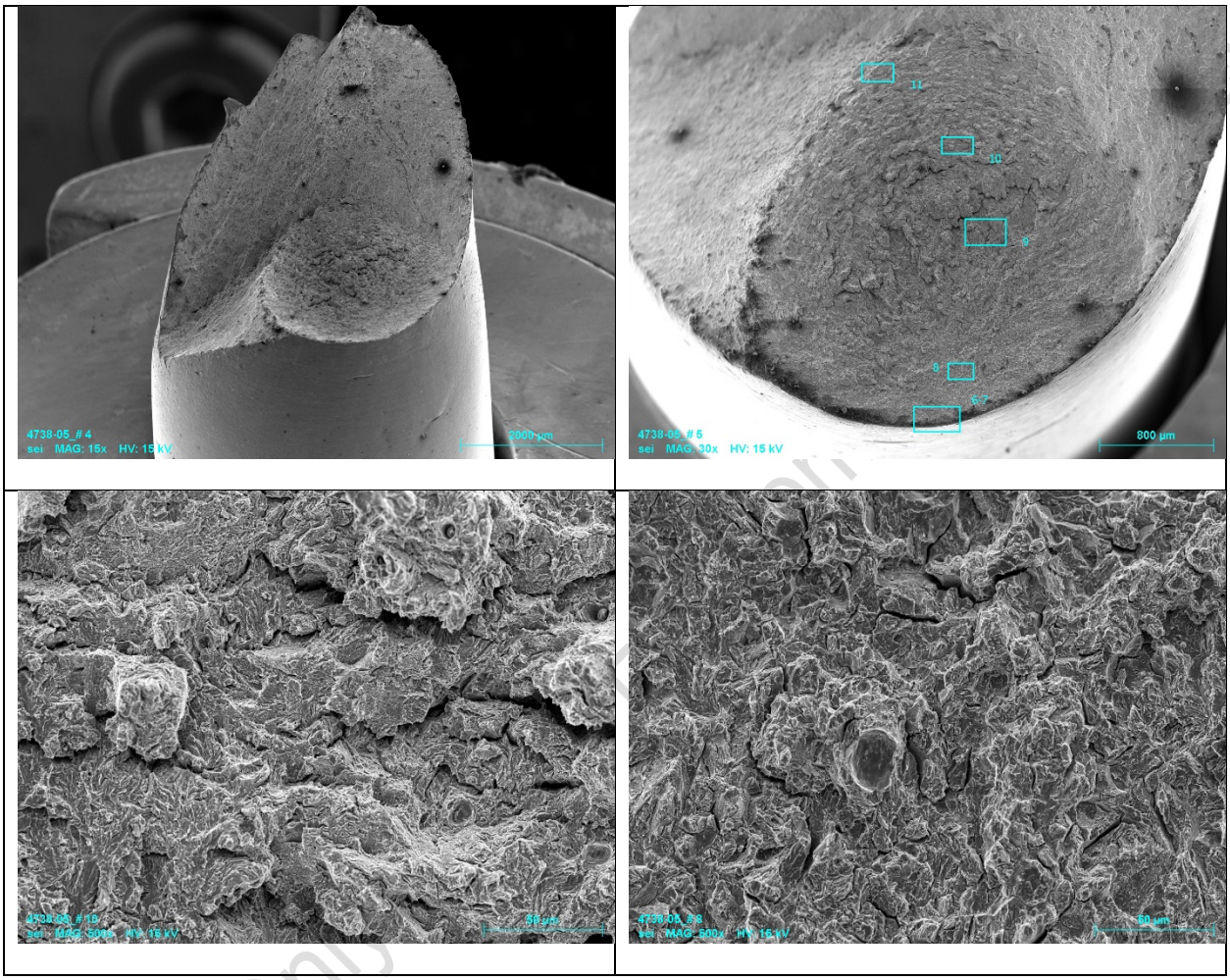

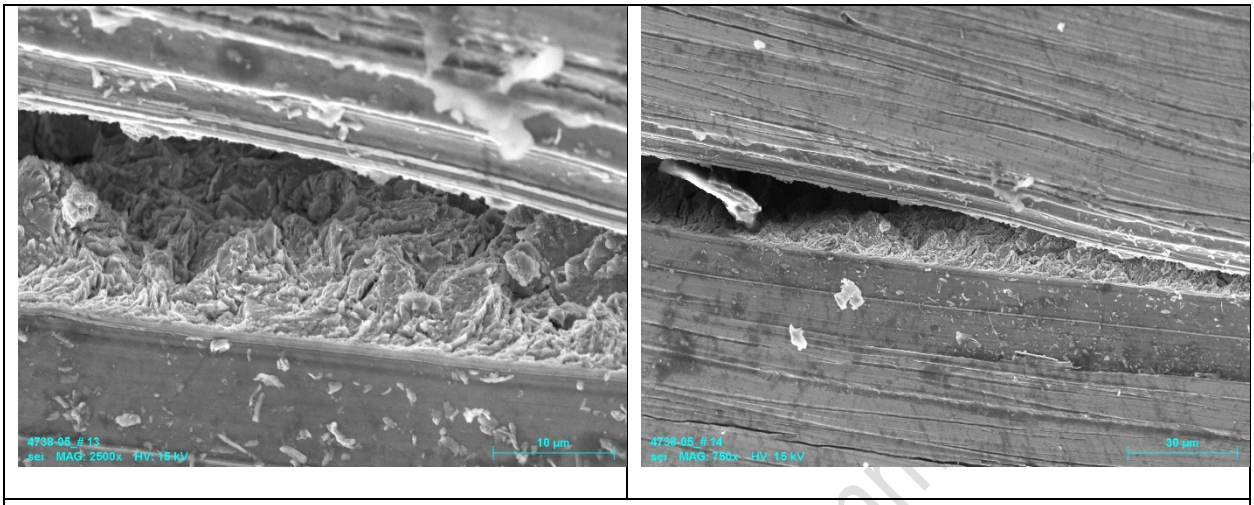

Figure 3 SEM photomicrographs of the SSR sample for 4140 steel tested in 100 bara hydrogen

The SSR results for 718-125K performed at strain rate of 10^{-5} s^{-1}. are summarized in Table 2. The hydrogen gas had limited effect on the ultimate tensile stress for the hydrogen gas tests relative to the Helium (inert) tests. A detrimental effect on material ductility was noted in high pressure H_2 by the decrease in both EL and RA in hydrogen gas.

Table 2. SSR testing results for 718-125K

Sample ID	Env.	0.2% Yield Stress (ksi)	UTS (ksi)	Elong. (%)	Red. of Area (%)	Avg. Elong. (%)	Avg. RA (%)	HEE EL (%)	HEE RA (%)
718-05	He	137	188	39.0	26.9	38.7	26.2	42.2	23.1
718-06	He	140	190	38.3	27.2				
718-07	He	138	189	38.7	24.6				
718-02	H_2	137	180	21.8	17.4	22.4	20.2		
718-03	H_2	140	183	21.8	21.1				
718-04	H_2	137	182	23.5	22.0				

The SEM photomicrographs of the 718-125K tested in He and in hydrogen are shown in Figures 4 and 5, respectively.

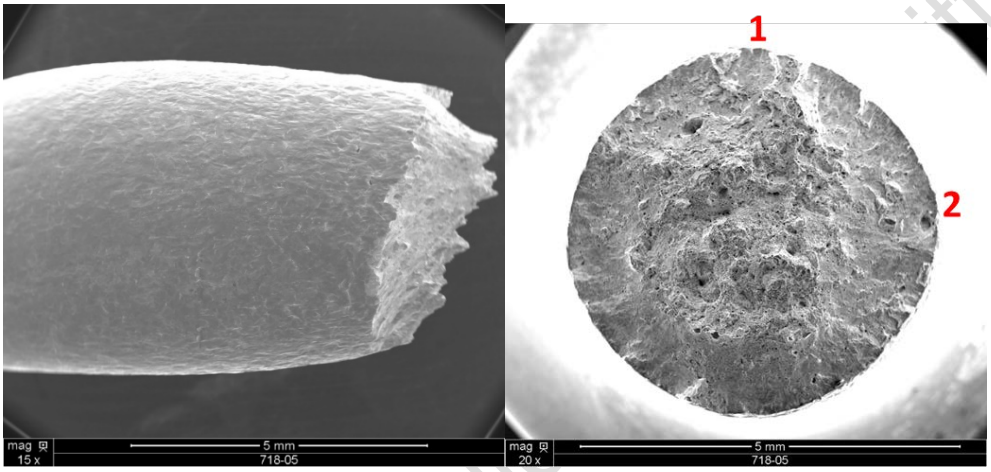

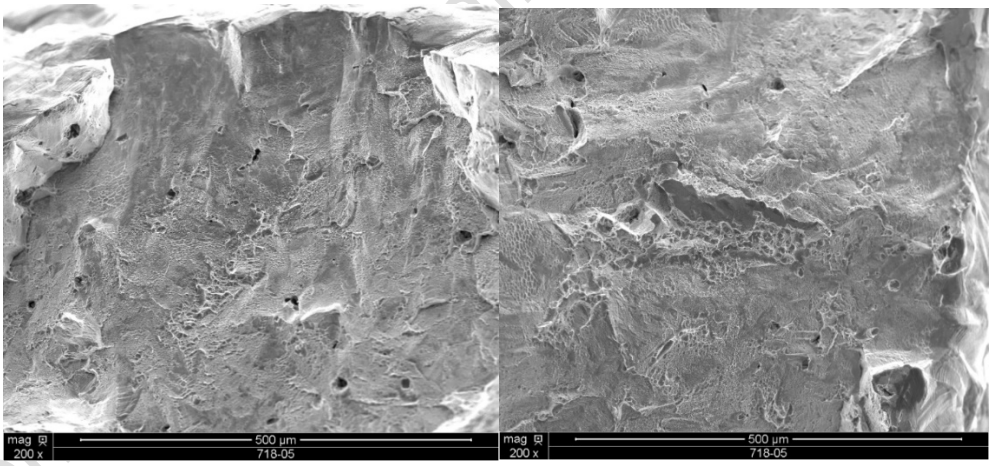

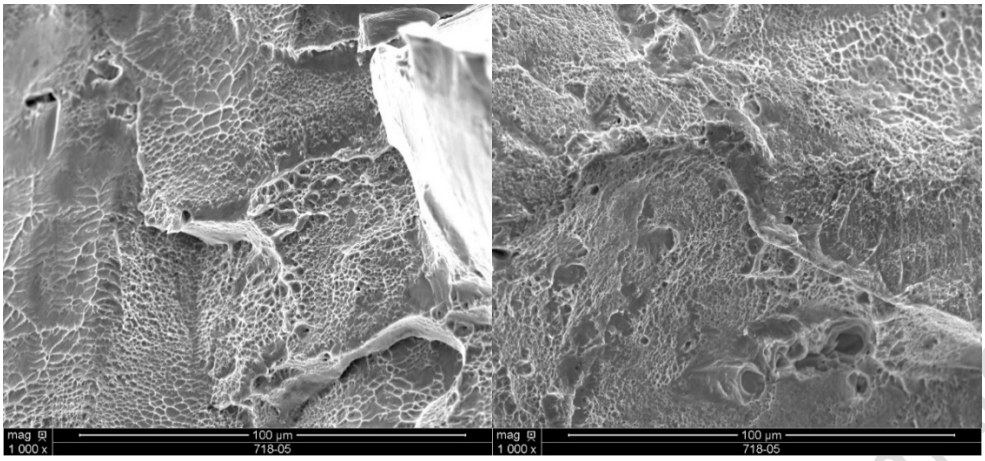

Figure 4 SEM photomicrographs of the SSR sample for Alloy 718 tested in nitrogen

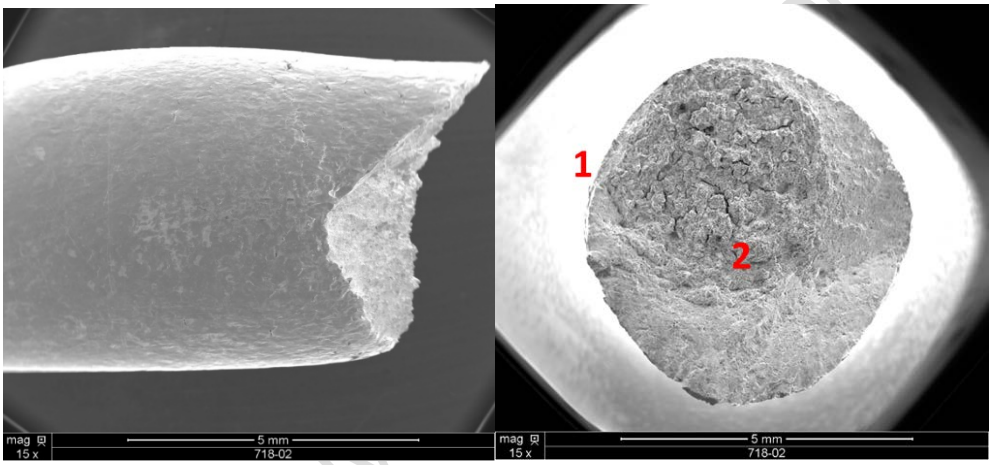

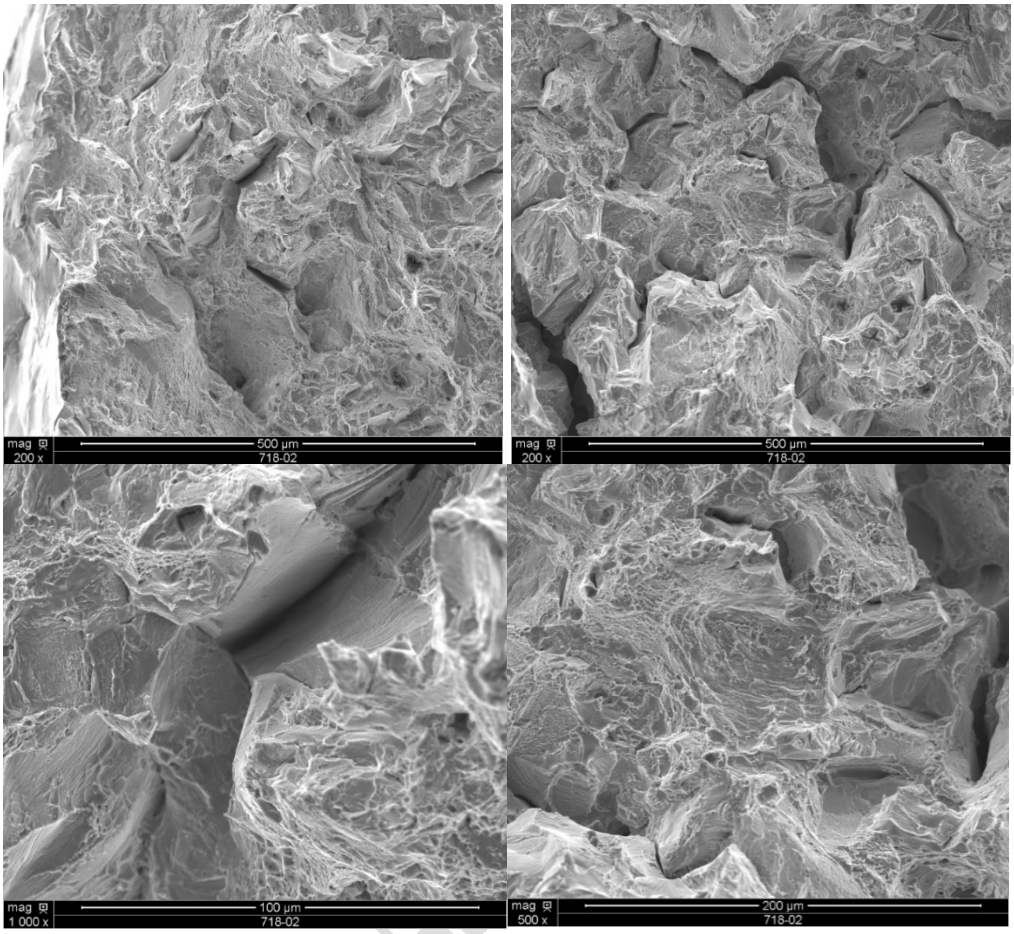

Figure 5 SEM photomicrographs of the SSR sample for *718-125*K tested in 100 bara H_2

5.3 FT Results

Alloy 718-125K and 4140-125K were tested for fracture toughness evaluation in an inert environment and in 100 bara gaseous hydrogen environment at two different labs (A, B). While the K-rate for H_2 was initially targeted as 0.01 $N.mm^{-3/2}.s^{-1}$; however, the tested K-rates for the tests in H_2 differed between the two labs. No specific K-rate for inert was specified as the K-values in inert are typically not rate dependent. At Test Lab A, all tests in inert environment (nitrogen) were performed under an initial K rate of approximately 3.8 $N.mm^{-3/2}.s^{-1}$ whereas the environmental tests were performed at an initial K rate of 0.01 $N.mm^{-3/2}.s^{-1}$. The inert environmental tests performed at Test Lab B were done under an initial K rate of ~12 $N.mm^{-3/2}.s^{-1}$. At test lab B the H2 tests on 718-125K performed were at an initial K rate of 0.02 $N.mm^{-3/2}.s^{-1}$ and the tests on 4140 steel were done at an initial K rate of 0.003 $N.mm^{-3/2}.s^{-1}$

The J-R curves for 718-125K can be found in the reports for the testing programs included in the Appendix A. The FT results obtained at the test labs are plotted as a function of the K rates and compared to the results obtained in the inert environments as well. The comparison is shown in Figure 6 6 for 718-125K. The comparison clearly showed the

significant reduction of the toughness in 100 bara hydrogen compared to the inert environment. The toughness values also showed clear dependency on the K rates at which the tests were performed. It should be noted that the tests at a given K-rate were performed in a given lab (i.e. both labs did not perform tests at both K-rates). Lower toughness values were observed at lower K rates, as shown in both Figure 6. This behavior is consistent with the behavior of 718 and low alloys steels in other hydrogen embrittling environments such as in seawater with cathodic protection. Typically, in those environments, the fracture toughness of low alloy steels reached a plateau value in the range of about 0.005 $N.mm^{-3/2}.s^{-1}$. In the case of alloy 718, the fracture toughness exhibited a decrease with K-rate even down to 0.005 $Nmm^{-3/2}.s^{-1}$. Hence it is not entirely surprising that the fracture toughness results in the current work, which were at K-rates of 0.01 and 0.02 $Nmm^{-3/2}.s^{-1}$for alloy 718 exhibit a K-rate dependence.

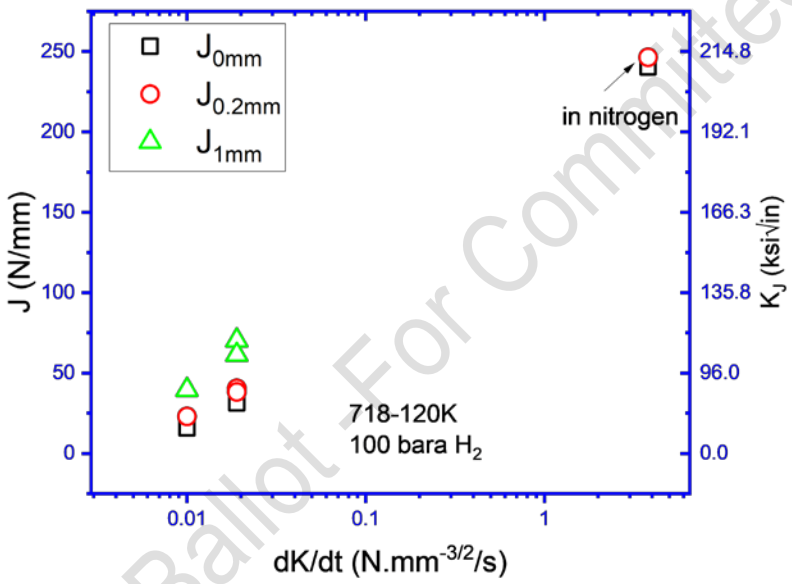

Figure 6 FT results as function of K rates for 718-125K in 100 bara hydrogen.

The FT results for 4140 steel from two labs are compared in Figure 7 as a function of the K rates. Similar to the results for 718-125K, the comparison clearly showed the significant reduction of the toughness for the two tested materials in 100 bara hydrogen compared to the inert environment. The toughness values also showed clear dependency on the K rates at which the tests were performed. The dependence of the fracture toughness of 4140 on K-rate is a bit surprising given that typically at the low K-rates tested the threshold values tend to reach plateau values. Some of the difference could be due to scatter and/or inter lab variability. It should be pointed out 4140 steel showed brittle behavior when tested in hydrogen. The samples broke into two halves with unstable crack extension at relatively low load values and thus J-R curves were not obtained for 4140 steel samples in hydrogen. Rather, elastic K_{IC} values were calculated following the instructions in ASTM E399 [25] /E1820 [26] for the samples tested in hydrogen.

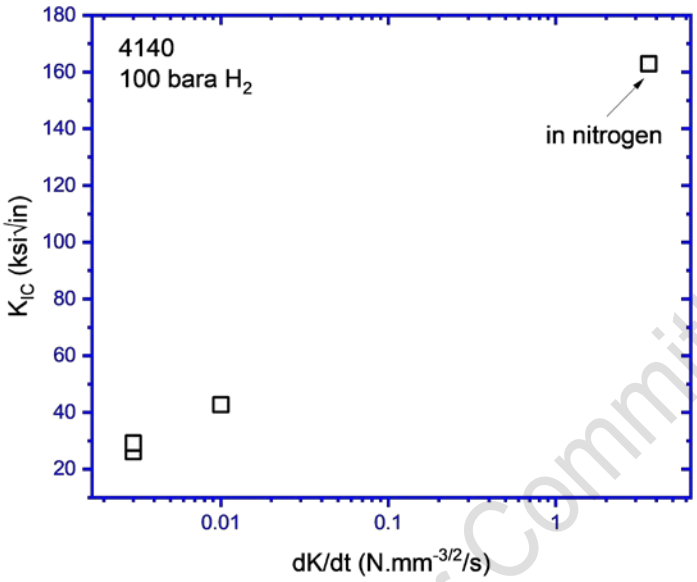

Figure 7 FT results as function of K rates for 4140 steel in 100 bara hydrogen.

The FT results are listed in Tables 3 and 4.

Table 3 Summary of FT results for 4140

Material	dk/dt ($N.mm^{-3/2}.s^{-1}$)	K_{IC} ($ksi.in^{1/2}$)	Test Lab
4140-125K	3.8	162.9	A
	0.01	42.7	A
	0.01	43.0	A
	0.003	30.1	B
	0.003	26.2	B
	0.003	26.2	B

Table 4 Summary of FT results for 718

Material	dk/dt ($N.mm^{-3/2}.s^{-1}$)	J_{0mm} ($N.mm^{-1}$)	$J_{0.2mm}$ ($N.mm^{-1}$)	J_{1mm} ($N.mm^{-1}$)	K_{J0mm} ($ksi.in^{1/2}$)	$K_{J0.2mm}$ ($ksi.in^{1/2}$)	K_{J1mm} ($ksi.in^{1/2}$)	Test Lab
718-125K	3.8	240.4	246.4		210.6	213.2		A
	0.01	15.8	23.0	39.5	53.9	65.2	85.4	A
	0.01	18.1	23.4	35.2	57.8	65.6	85.6	A
	0.02	33.8	40.5	70.3	78.9	86.4	113.9	B
	0.02	31.3	38.2	61.4	76.0	83.9	106.4	B

5.4 Hydrogen Permeation Results

The hydrogen flux experimental setup at one test lab was validated by performing a hydrogen permeation test using 3.5% NaCl (pH 8.2) on the charging side of the setup. A cathodic potential of -1050 mV vs. SCE was applied to the sample on the charging side which was an X52 line pipe steel. The oxidation side was the typical 0.1 M NaOH solution and was maintained at +300 mV vs. saturated calomel electrode (SCE). The purpose of this test was to make sure the use of a metal autoclave on the charging side, and the use of the fixtures mounting the sample to hold pressure, did not interfere with any hydrogen uptake or the measurements. The flux transient from this validation test is shown in Figure 8. The red line is the numerical fitted line based on the solution to a one-dimensional diffusion and the symbols are the experimental data. As shown, the experimental data and the fitted line agreed very well and the effective diffusion coefficient of hydrogen in the tested material was $9.4x10^{-8}$ $cm^2.s^{-1}$. The experimental results confirmed that the experimental setup is capable of measuring the hydrogen that diffuses through the sample.

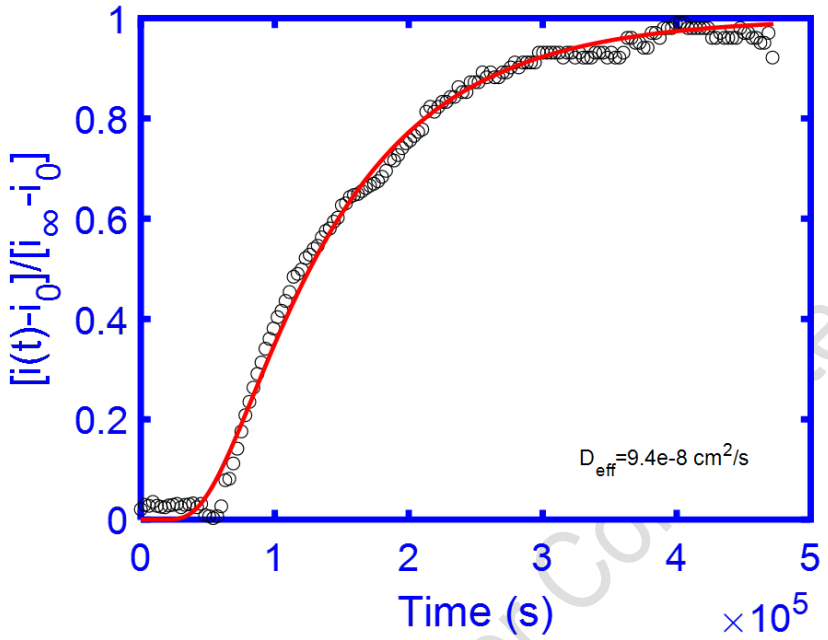

Figure 8 The flux transient as a function of time for the test in 3.5% NaCl solution at pH 8.2

Figure 9 shows the oxidation current as a function of time for the hydrogen flux test that was performed for this project on 4140 steel sample. Prior to exposing the sample to hydrogen for about 46.5 hours, a background current density lower than 100 nA/cm^2 was established on the oxidation side (exposed to 0.1 M NaOH and polarized to 0.3 V vs. SCE). Hydrogen pressure on the charging side was established at 46.5 hours. Typically, the oxidation current then would rise if hydrogen diffused through the sample exposed to 0.1 M NaOH at +300 mV vs. SCE, like what was shown in Figure 7. However, throughout the whole duration of flux test conducted using 1450 psia hydrogen, which lasted for about 720 h, the current density remained low in the range of 100 nA/cm^2. The lack of a current rise or a transient suggests that no detectable hydrogen was diffusing through the sample. These results are consistent with the experience of the test lab in other projects which did not detect any diffused hydrogen either in hydrogen charging conditions similar to this project. This is not surprising since gaseous hydrogen would have to undergo adsorption and dissociation before entering steels. Such processes are favored on surfaces where the oxide is disrupted which is absent on the statically exposed samples.

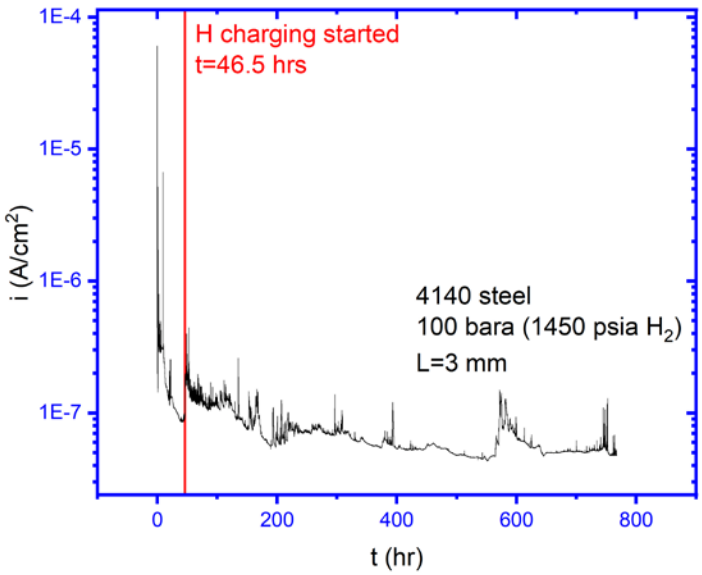

Figure 9. Oxidation current vs. time for the test with 4140 steel

The results for the permeation testing for 718-125K with 1450 psia hydrogen gas are shown in10. The figure shows the permeation current density versus time. Low background currents were observed initially (nA range). The hydrogen charging pressure was introduced at 30 hours after the solution in the oxidation cell was transferred. Testing was ongoing for more than three weeks and no increase in the current was observed suggesting the lack of hydrogen breaking through within the duration of testing. It should be noted that the sample thickness for this exposure was 0.118 inches (0.3 cm). Assuming that entry of hydrogen was a not a limiting factor and a diffusion co-efficient of 2×10^{-11} cm^2/s for alloy 718 at RT[23], the breakthrough time for a 0.3 cm thick specimen would be on the order of 35 years. Thus, it may have been more beneficial to have tested a much thinner sample which should be sized using hydrogen diffusivity found in the literature for 718.

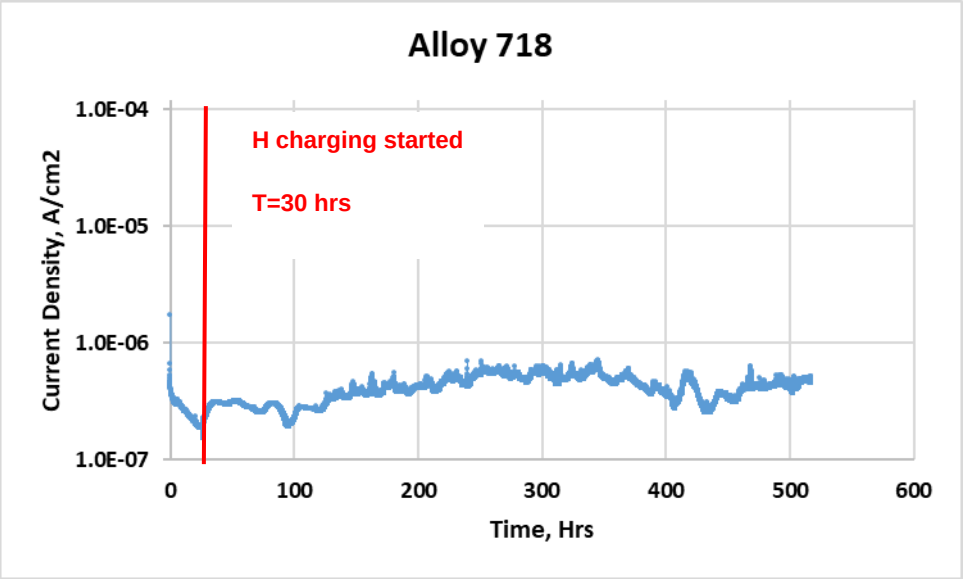

Figure 10. Hydrogen permeation measurements for the Alloy 718

6 Discussion

6.1 General

The results of the test program provide measures of susceptibility to hydrogen embrittlement for the materials tested. The results in hydrogen for the two materials from the different test methods are used to understand the role of test method and material type on the susceptibility to hydrogen embrittlement in high pressure H_2.

6.2 Comparison of Materials

The SSR results for both materials showed a decrease in the strain failure and reduction in area in high pressure H_2 compared to inert environments. A comparison of the parameters from the SSR tests for both materials is shown in Figure 11.

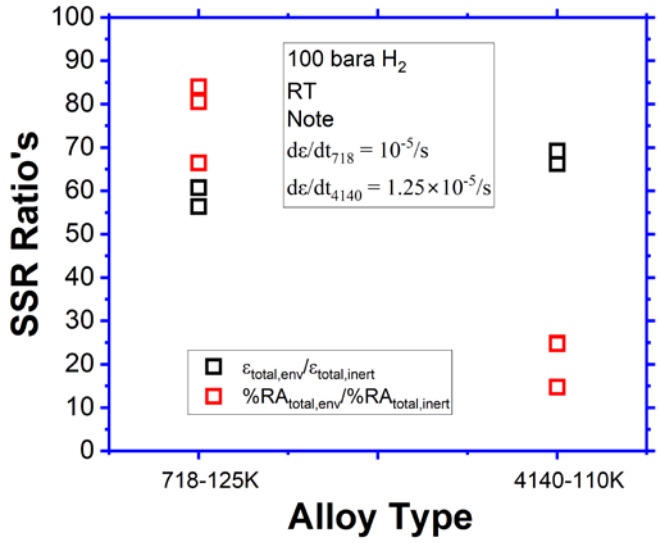

Figure 11 Comparison of the SSR performances in 100 bara H_2 at RT

The comparison clearly suggests that the decrease in %RA (relative to the inert environment) for 4140-125K is significantly higher than for alloy 718-125K, even though the change in %ε (relative to the inert environment) is similar for both materials. The results suggest that even though the yield strength of the alloys is similar (~140 ksi) the response in the SSR tests is very different, highlighting the difference between the alloy classes.

A comparison of the K_{th} (as defined by J at the onset of crack extension) for the alloys is shown in Figure 12. The results clearly indicate that the K_{th} of alloy 718 is significantly higher than that of 4140 across the K-rates tested, though it is possible that at very low K-rates the K_{th} of alloy 718 may be lower than the values measured at 0.01 $Nmm^{-3/2}/s$ (the lowest K-rate tested). In addition, to the higher values of K_{th}, alloy 718 exhibited stable crack propagation, while 4140 exhibited unstable crack propagation. This indicates that not only was the K_{th} of 718 higher but the crack growth rate was lower.

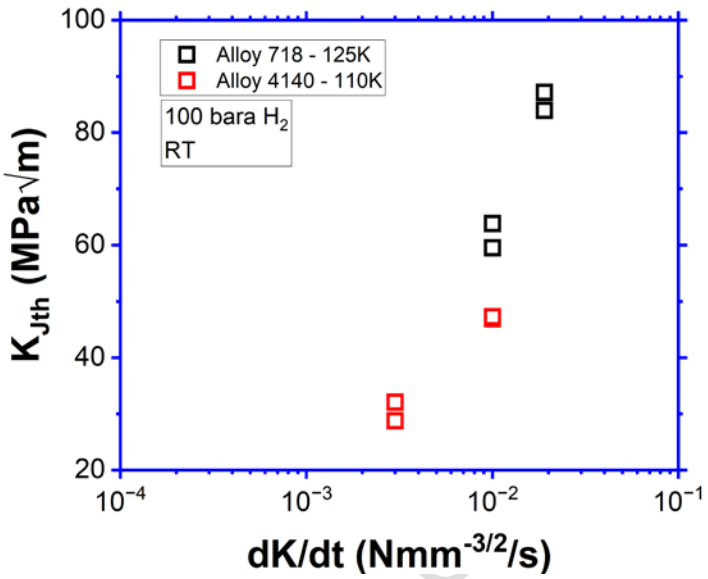

Figure 12 Comparison of the K_{th} values of the two alloys tested in 100 bara H_2 at RT.

6.3 Relationship Between Hydrogen Permeation and Embrittlement

It is interesting to point out that although SSR and FT results in high pressure H_2 were significantly lower for both 4140 steel and 718 in 100 bara hydrogen, the hydrogen flux measurements did not indicate any measurable hydrogen breakthrough for either material. As indicated in the earlier section, even if hydrogen uptake occurred immediately upon exposure, no breakthrough would be observed on alloy 718 for about 35 years on account of the low diffusion co-efficient with the thickness of the sample that was tested. For 4140 steel, though, given the significantly higher diffusion coefficient in the range of 10^{-7} cm^2/s, if hydrogen update occurred, it is expected that diffusion through a 0.3 cm membrane would occur within 2 to 3 days.

The significant influence of hydrogen on the K_{th} and % RA for both materials in the absence of any hydrogen uptake in the permeation measurements suggests the hydrogen uptake occurred locally at the deformation site. In addition to facilitating damage accumulation, plastic deformation may disrupt the oxide and expose fresh metal, which may facilitate hydrogen dissociation and uptake.

It is therefore important to note that a better understanding of the dissociation of molecular H_2 on both oxide surfaces and fresh metal surfaces is needed to understand the relationship between hydrogen uptake and the embrittlement behavior. In particular, it is important to understand if the process of dissociation of molecular H_2 on oxide surfaces is thermodynamically limited or kinetically limited. There is work in literature suggesting that oxides can be reduced in the presence of molecular H_2 at elevated temperatures (>80°C). Once the oxide is reduced at elevated temperature, H_2 dissociation and subsequent entry occurs even when the temperature is lowered to room temperature[24]. In light of these observations, it is important to understand if over extended periods of materials exposure to gaseous hydrogen expected in real-life applications, if it is possible for molecular H_2 to dissociate and ingress.

6.4 Influence of Loading Parameters

The FT results also demonstrate that the toughness values of the materials are sensitive to the tested K rate. In the current work among the K-rates tested for both materials, no plateau in K_{th} was observed. Though, it should be noted some of the differences in K_{th} at different K-rates, may be attributed to the tests at different K-rates being performed at different laboratories.

In order to better understand the effect of K-rate, one of the labs performed an additional test internally at constant K conditions. The procedure to establish constant K conditions is based on work performed in several JIPs. The results of the constant K tests at 49.5 MPa.m$^{1/2}$ is shown in Figure 13. A very slow SCGR of 2×10^{-9} mm.s^{-1} appears to be evident under constant K conditions.

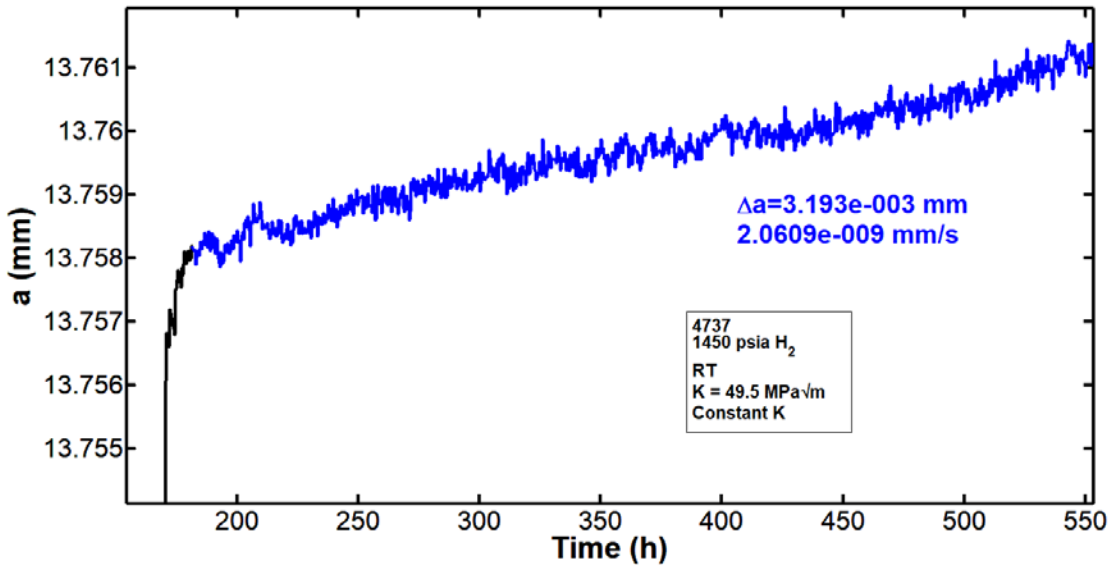

Figure 13 Crack growth rate under constant K conditions (K = 49.5 MPa.m$^{1/2}$) for alloy

The SCGR at 60.5 MPa.m$^{1/2}$ under constant K conditions is shown in Figure 15. The SCGR is about 2.6×10^{-6} mm.s^{-1}, a 1000 fold increase from the SCGR at 49.5 49.5 MPa.m$^{1/2}$ suggesting that the K_{th} is about 49.5 MPa.m$^{1/2}$ under constant K conditions.

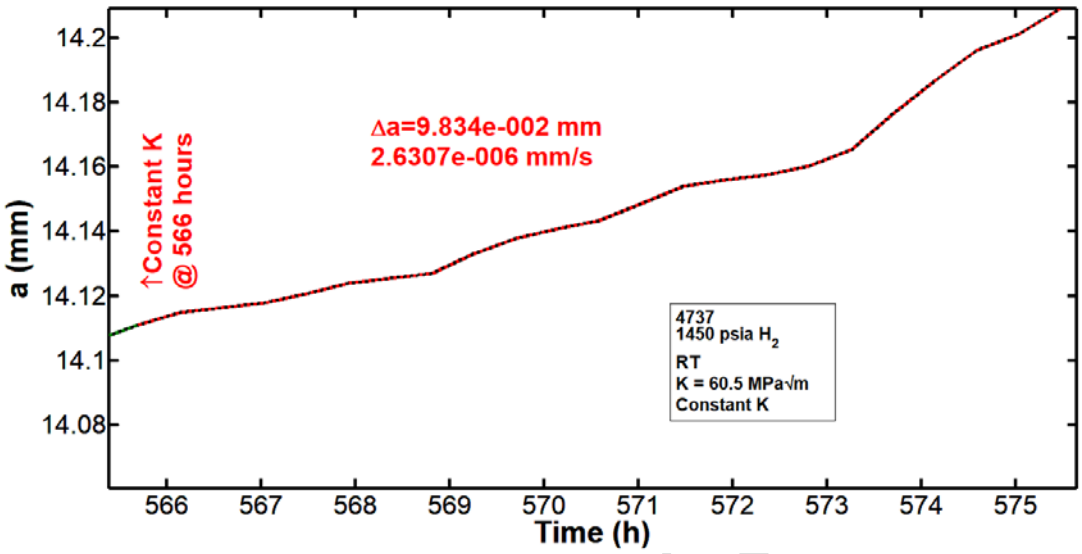

Figure 15 Crack growth rate under constant K conditions (K = 60.5 MPa.m$^{1/2}$) for alloy 718

The results of the constant K tests performed by one test lab help understand the role of K-rate on the K_{th} behavior of alloy 718 in high pressure H_2. A summary of the effect of K-rate on the measured K_{th} for alloy 718 is shown in Figure 16. These results indicate that for alloy 718 under these conditions, the constant K conditions appear to provide lower bound K_{th} values. It is possible that slow rising displacement at K-rates of 0.005 Nmm$^{-3/2}$.s^{-1} or lower may provide a sufficiently low K-rate to provide lower bound values of K_{th}. This emphasizes the need to use low K-rates to obtain lower bound K_{th} values for structural integrity values.

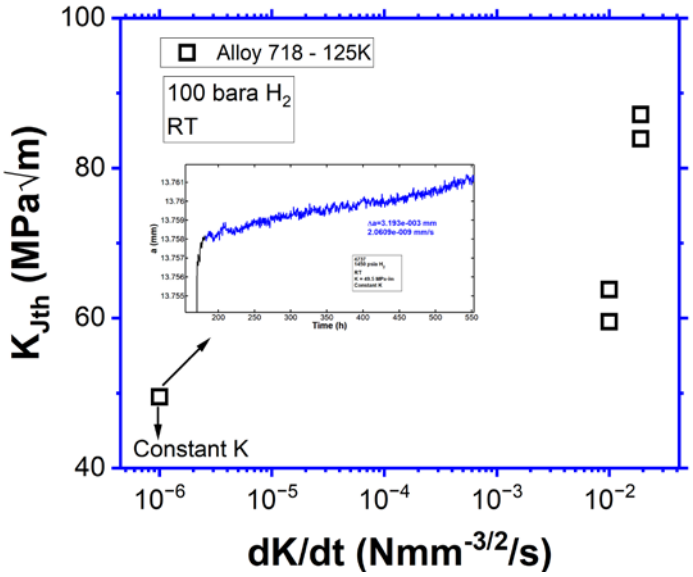

Figure 16 Effect of K-rate on the K_{th} behavior of alloy 718 in 100 bara H_2 at RT.

Hence, for structural applications it is important to understand the loading profile that the component would encounter in relevant applications. For instance, for underground high pressure hydrogen storage application, the loading on the structural component may often subject to constant high mean loads coupled with occasional ripple loads. These low amplitude ripple loads are associated with filling and drawing from the storage wells based on demand of hydrogen. Start up and shut down, though, may impose deep unload/reload events on the components in the storage wells.

Therefore, in addition to understand the fracture properties of the materials that are used in the storage applications, it is critical to understand the crack growth behavior under relevant loading conditions, such as constant K conditions coupled with ripples. For underground hydrogen storage application, the materials will likely be exposed to a hydrogen environment that contains impurities such as water, oxygen and H_2S, to name a few. As discussed in previous sections, other studies have shown that the presence of these impurities have effect on hydrogen embrittlement of material with some of them being beneficial (e.g., oxygen) but some of them can be detrimental (e.g., water in some cases). Therefore, for a given material and a given application, a comprehensive understanding of the material properties will need to consider not only the representative loading scenarios but also the representative environmental conditions.

Bibliography

[1] N. S. Muhammed, B. Haq, D. Al Shehri, A. Al-Ahmed, M. M. Rahman, and E. Zaman, "A review on underground hydrogen storage: Insight into geological sites, influencing factors and future outlook," *Energy Reports,* vol. 8, pp. 461-499, 2022/11/01/ 2022, doi: https://doi.org/10.1016/j.egyr.2021.12.002.

[2] E. R. Okoroafor, S. D. Saltzer, and A. R. Kovscek, "Toward underground hydrogen storage in porous media: Reservoir engineering insights," *International Journal of Hydrogen Energy,* vol. 47, no. 79, pp. 33781-33802, 2022, doi: 10.1016/j.ijhydene.2022.07.239.

[3] B. Pan, X. Yin, Y. Ju, and S. Iglauer, "Underground hydrogen storage: Influencing parameters and future outlook," *Adv Colloid Interface Sci,* vol. 294, p. 102473, Aug 2021, doi: 10.1016/j.cis.2021.102473.

[4] R. Walter and W. Chandler, "Influence of gaseous hydrogen on metals," 1973.

[5] R. Jewett, R. Walter, and W. Chandler, "Influence of high pressure hydrogen on cyclic load crack growth in metals," in *Corrosion-Fatigue Technology*: ASTM International, 1978.

[6] N. Moody, M. Perra, and S. Robinson, "Hydrogen pressure and crack tip stress effects on slow crack growth thresholds in an iron-based superalloy," *Scripta Metallurgica,* vol. 22, no. 8, pp. 1261-1266, 1988.

[7] C. San Marchi, J. Ronevich, P. Bortot, Y. Wada, J. Felbaum, and M. Rana, "Technical Basis for Master Curve for Fatigue Crack Growth of Ferritic Steels in High-Pressure Gaseous Hydrogen in ASME Section VIII-3 Code," in *ASME 2019 Pressure Vessels & Piping Conference*, 2019: American Society of Mechanical Engineers Digital Collection.

[8] K. A. Nibur, B. P. Somerday, C. San Marchi, J. W. Foulk, M. Dadfarnia, and P. Sofronis, "The relationship between crack-tip strain and subcritical cracking thresholds for steels in high-pressure hydrogen gas," *Metallurgical and Materials Transactions A,* vol. 44, no. 1, pp. 248-269, 2013.

[9] J. A. Ronevich, E. J. Song, B. P. Somerday, and C. W. San Marchi, "Hydrogen-assisted fracture resistance of pipeline welds in gaseous hydrogen," *International Journal of Hydrogen Energy,* 2021/01/19/ 2021, doi: https://doi.org/10.1016/j.ijhydene.2020.11.239.

[10] C. San Marchi and B. P. Somerday, "Technical reference on hydrogen compatibility of materials," in "Sandia National Laboratories, SANDIA REPORT SAND2008-1163," 2008.

[11] G. L. Pioszak and R. P. Gangloff, "Hydrogen environment assisted cracking of modern ultra-high strength martensitic steels," *Metallurgical and Materials Transactions A,* vol. 48, no. 9, pp. 4025-4045, 2017.

[12] R. P. Gangloff, "H-Enhanced Deformation and Fracture in the Crack Tip Process Zone," in *International Hydrogen Conference (IHC 2016): Materials Performance in Hydrogen Environments*, 2017: ASME Press.

[13] N. Bandyopadhyay, J. Kameda, and C. McMahon, "Hydrogen-induced cracking in 4340-type steel: effects of composition, yield strength, and H 2 pressure," *Metallurgical Transactions A,* vol. 14, no. 4, pp. 881-888, 1983.

[14] N. Bandyopadhyay and C. McMahon, "The micro-mechanisms of tempered martensite embrittlement in 4340-type steels," *Metallurgical Transactions A,* vol. 14, no. 7, pp. 1313-1325, 1983.

[15] C. J. McMahon, "Hydrogen-induced intergranular fracture of steels," *Engineering Fracture Mechanics,* vol. 68, no. 6, pp. 773-788, 2001/04/01/ 2001, doi: https://doi.org/10.1016/S0013-7944(00)00124-7.

[16] T. Perng and C. Altstetter, "Comparison of hydrogen gas embrittlement of austenitic and ferritic stainless steels," *Metallurgical Transactions A,* vol. 18, no. 1, pp. 123-134, 1987.

[17] T. P. Perng and C. J. Altstetter, "Cracking kinetics of two-phase stainless steel alloys in hydrogen gas," *Metallurgical Transactions A,* vol. 19, no. 1, pp. 145-152, 1988/01/01 1988, doi: 10.1007/BF02669823.

[18] W. Clark and J. Landes, "An evaluation of rising load K ISCC testing," in *Stress Corrosion—New Approaches*: ASTM International, 1976.

[19] B. P. Somerday and K. A. Nibur, "Effect of Applied K Level on the Crack-Arrest Threshold in Hydrogen Environments: Mechanics-Based Interpretation," *CORROSION,* vol. 75, no. 8, pp. 929-937, 2019, doi: 10.5006/3106.

[20] N. R. Moody, M. I. Baskes, S. L. Robinson, and M. W. Perra, "Temperature effects on hydrogen-induced crack growth susceptibility of iron-based superalloys," *Engineering Fracture Mechanics,* vol. 68, no. 6, pp. 731-750, 2001/04/01/ 2001, doi: https://doi.org/10.1016/S0013-7944(00)00122-3.

[21] T. P. Perng and C. J. Altstetter, "Effects of water vapor on hydrogen induced slow crack growth in stainless steels," *Metallurgical Transactions A,* vol. 19, no. 3, pp. 651-656, 1988/03/01 1988, doi: 10.1007/BF02649279.

[22] T.-P. Perng and C. J. Altstetter, "Effects of water vapor and hydrogen sulfide on hydrogen permeation in stainless steels," *Acta Metallurgica,* vol. 36, no. 5, pp. 1251-1260, 1988/05/01/ 1988, doi: https://doi.org/10.1016/0001-6160(88)90277-5.

[23] W. M. Robertson, "Hydrogen permeation and diffusion in inconel 718 and incoloy 903," *Metallurgical Transactions A,* journal article vol. 8, no. 11, pp. 1709-1712, November 01 1977, doi: 10.1007/bf02646873.

[24] A. Nagao, S. Takagi, N. Ishikawa, and M. Kimura, "Hydrogen Uptake in Steels Exposed to High-Pressure H2 Gas," in *International Hydrogen Conference (IHC 2016): Materials Performance in Hydrogen Environments*, B. P. Somerday and P. Sofronis Eds.: ASME Press, 2017, p. 0.

[25] ASTM E399, 2023, 'Standard Test Method for Line-Elastic Plane-Strain Fracture Toughness of Metallic Materials', ASTM

[26] ASTM E1820, 2013: 'Standard Test Method for Measurement of Fracture Toughness', Edition 13, ASTM

Appendix A: Experimental Details for API Material Testing in Hydrogen from Test Lab A

1 TEST MATERIALS AND SPECIMENS

1.1 Materials

The materials tested in the project were provided by API. The provided 718 and 4140 steel were assigned Lab A identification number (ID) of 4737 and 4738, respectively, as shown in Figure 1. Both materials were provided as a bar form with 12 inch in length and 5 inch in outer diameter (OD) for alloy 718 - 120K and 17 inch in length and 5 inch in OD for 4140 steel. Longer material was provided for 4140 steel due to the need of machining SSR samples and flux samples. Table 1 shows a summary of the material dimensions and the mechanical properties. The MTRs of the materials are included in Appendix A.

Table 3. Dimensions and mechanical properties of supplied materials.

Material	Lab A ID	Diameter (in)	Length (in)	Yield Strength (ksi)	Tensile Strength (ksi)
718	4737	5	12	135.2	181.8
4140	4738	5	17	137.0	154.4

1.2 Specimen

Compact tension (CT) specimens were used to perform FT testing and were extracted from the provided materials at the mid-radius location (Figure 2). The samples were notched in the C-L orientation with the crack growing along the longitudinal direction of the bar, as shown in Figure 3.

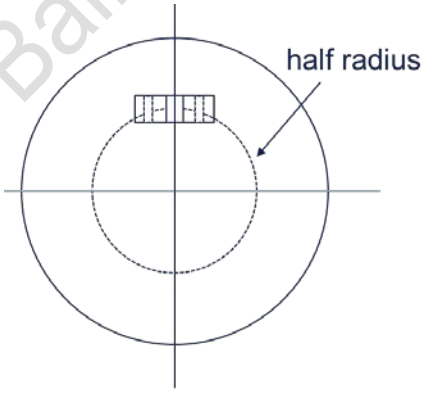

Figure 2. Illustration of sample extraction location for the CT fracture toughness samples.

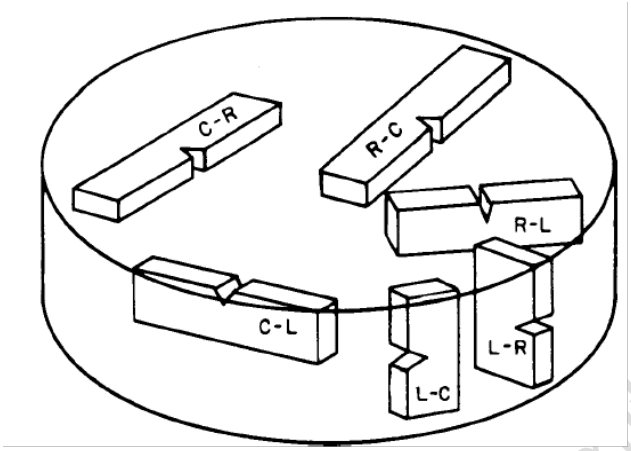

Figure 3. Schematic illustration of notch orientation in a hollow bar or cylinder /1/.

A schematic of the CT fracture toughness specimen (referred as JCT) is shown in Figure 4. The samples were machined to the following dimensions:

- Specimen width, W=1″.
- Specimen thickness, B=0.5″.
- Initial a/W = 0.5 (where a is the total crack length including the pre-crack. Nominal notch depth 0.45 inch with 0.05 inch precracking in air)
- Specimens were side grooved by 5% of the thickness on each side. The samples were side grooved prior to precracking.

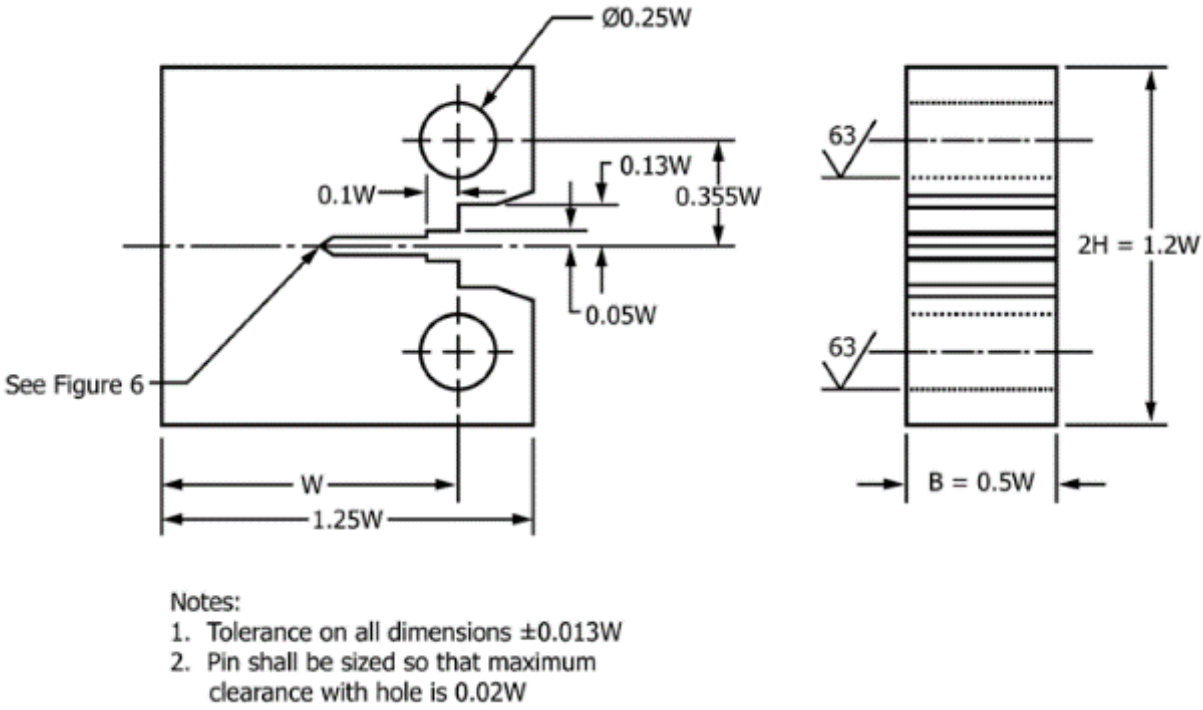

Figure 4. Schematic of the FT CT specimens (ASTM E1820 /2/).

The samples were precracked in air to an initial a/W of 0.5 under a constant K_{max} of 25 ksi√ in (27.5 MPa√ m) with R rations varying from 0.2 to 0.4 and at 2 Hz. The last 15 mils of the precracking were performed under a ΔK of 15 ksi√ in (16.5 MPa√ m). All precracking was done at Lab A.

SSR tests were performed for 4140 steel using the button head SSR samples. An example schematic of the button head SSR sample is shown in Figure 5. Similar to the JCT samples, SSR samples were also extracted from the mid-radius location of the 4140 steel bar.

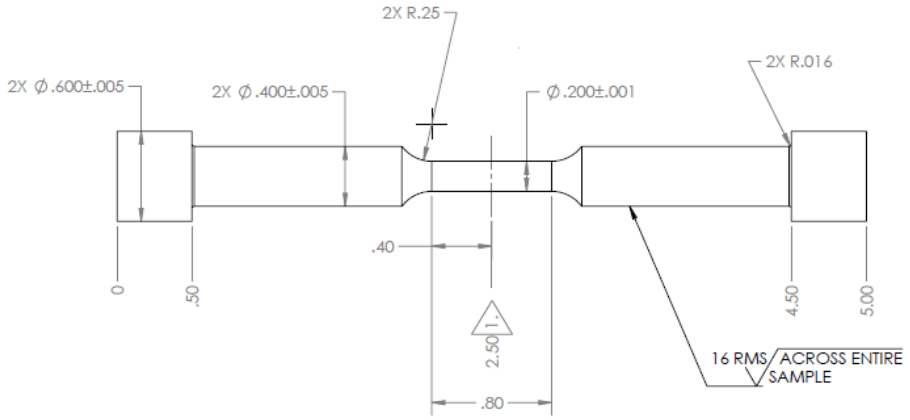

Figure 5. Schematic of the button head SSR sample

2 Test Matrix

Table 2 lists the tests that were performed in the project, including the FT tests, SSR tests and the hydrogen flux test.

Table 4. Test matrix

Material	Type of Testing	Environment	Number of Tests
Lab A ID 4737 (718)	FT	100 bara nitrogen	1
		100 bara hydrogen, measure oxygen and moisture	2
Lab A ID 4738 (4140)	FT	100 bara nitrogen	1
		100 bara hydrogen, measure oxygen and moisture	2
	SSR	100 bara nitrogen	3
		100 bara hydrogen, measure oxygen and moisture	3
	H flux	100 bara hydrogen, measure oxygen and moisture	1

3 Approach

The tests in this project were performed using 100% hydrogen to study the environmental effect and in nitrogen to establish the baseline performance in inert environment. All tests were performed at a total pressure of 100 bara and at room temperature.

3.1 FT Testing

3.1.1 Test Setup

All FT tests were performed in C276 autoclaves installed on servo electric frames. The setup was designed to handle the total test pressure as well as control oxygen to less than 1 pmm in the test. An example setup is shown in Figure 6.

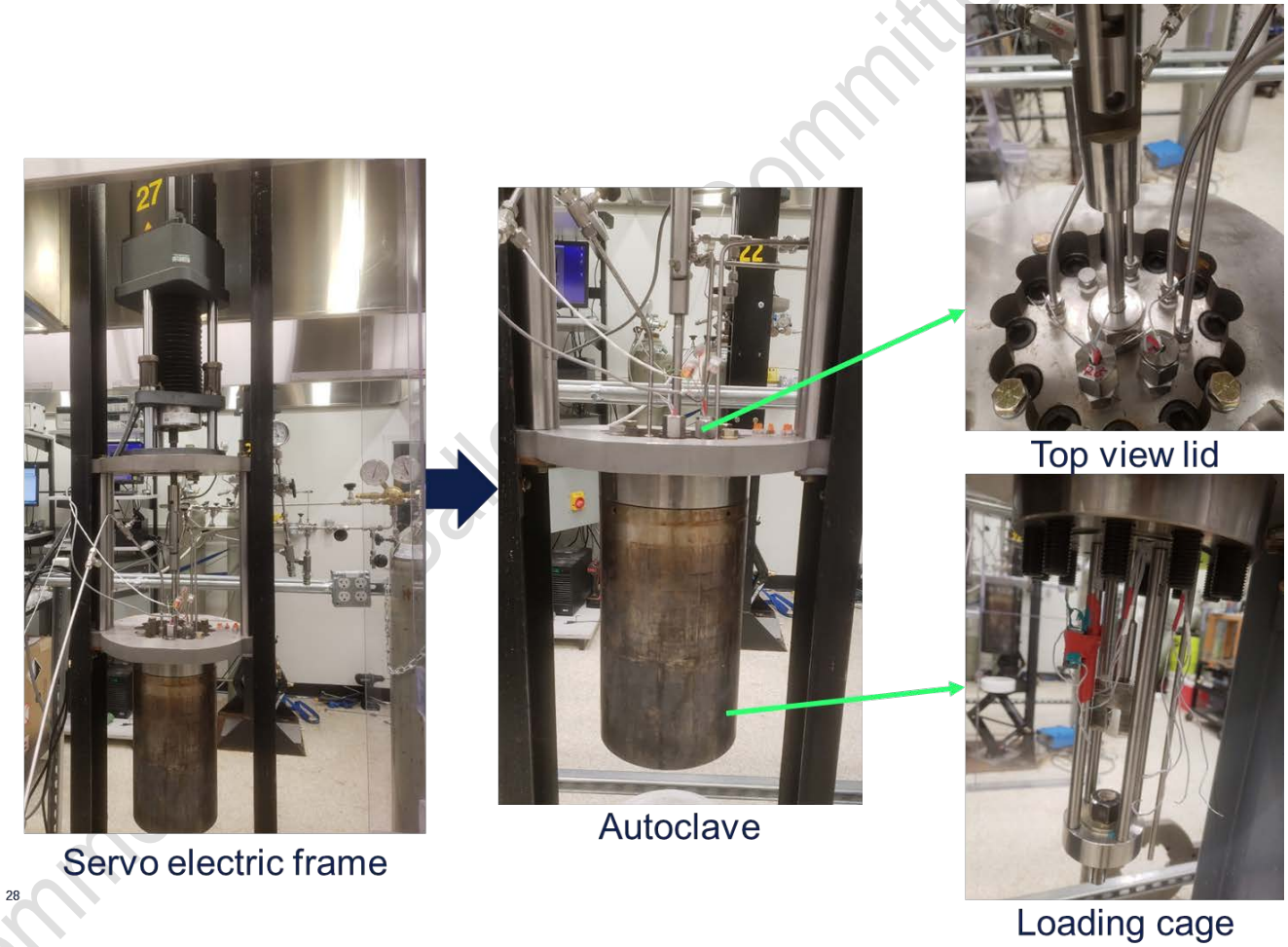

Figure 6. Test set up showing the test frame, autoclave and the gas cylinders.

3.1.2 Autoclave Charging Procedure

FT tests were performed in C276 autoclaves with 100 bara of hydrogen gas pressure at room temperature. The CT sample was electrically isolated from the autoclave, and the test frame, to prevent ground loops affecting the crack growth measurements. The autoclaves were assembled with the CT sample to be tested, sealed and pressure tested overnight at 2000 psig. After the pressure test, the autoclave/sample was purged with high purity nitrogen overnight to reduce moisture. lave. This was followed by cycles of 150 psig nitrogen and vacuum to remove nitrogen from the previous step. This pressure-release cycle was repeated five more times to minimize oxygen in the system. This was followed by pressurization of the autoclave with test gas – 100% hydrogen to 150 psig and vacuuming out the filled hydrogen. This pressure-release cycle was repeated one more time. This step was followed by flowing the test gas through the autoclave at a pressure of 500 psig at a flow rate of about 0.5 scfh. The gas outlet from the autoclave was connected to an oxygen analyzer. The lines connecting the sensor to the autoclave were also preconditioned using the nitrogen/vacuum and hydrogen/vacuum cycles. Once the oxygen concentration reached below 1 ppm, the autoclave was pressurized to 100 bara and all valves connecting to gas tanks were closed. Along with the oxygen sensor, there was a moisture analyzer connected to the autoclave to confirm that the moisture was low enough to validate all results obtained. The system was allowed to stabilize for at least 2 hours before loading the sample at the displacement rate. At the conclusion of the test, the pressure of the autoclave was brought down to ambient by releasing the gas through the oxygen analyzer to ensure that the oxygen stayed below 1 ppm during the test.

3.1.3 Rising Displacement Fracture Toughness Testing

FT tests were performed under displacement control at a low initial K-rate to capture the environmental effect. The test in nitrogen were performed at a displacement rate of $1x10^{-4}$ in/s corresponding to a K rate of 3 to 4 $N{\cdot}mm^{-3/2}/s$. The tests in nitrogen not only help establish the baseline performance of the materials in an inert environment but also help establish the displacement rate that is required to achieve the K rate for the tests in hydrogen.

The FT rising displacement testing parameters for the tests in hydrogen are summarized below:

Tested Materials: 718-125K and 4140

Notch Location: Base metal

Test method: Rising displacement

- Initial K-rate: ~1 $MPa\sqrt{m}$/hr (0.01 $N.mm^{-3/2}/s$)

The crack mouth opening displacement (CMOD) for all the rising displacement FT tests was determined by correcting the load line displacement with the frame stiffness for the given sample geometry and temperature. The details of the CMOD determination are included in Appendix B of this document.

3.1.4 Crack Length Measurement

The crack length in all tests were measured *in-situ* using the Direct Current Potential Drop (DCPD) technique. A constant current of 4 amp was used for DCPD crack length monitoring and the voltage drop across the crack mouth was measured using a high resolution digital multi-meter. The polarity of the current was frequently alternated during each DCPD data point measurement. This was done to eliminate thermal junction potentials in the system and improve the accuracy of DCPD. Ni wires encased in PTFE heat shrink sleeves were used for the current and voltage signals. The spot weld locations of the probes on the samples were coated (using 3M Scotchkote™ 323 liquid epoxy) as a strain relief. The measured voltage drop was converted into crack length using the Johnson equation (equation A1.2 in ASTM E1457 /3/). The voltage drop, as well as the converted crack length, were recorded using a Labview® program.

3.1.5 Specimen Examination

Upon completing the FT tests, all specimens were removed from the autoclaves and broken open to examine the fracture surface using a stereomicroscope for:

- Measurement of the actual initial and final crack length.

3.2 SSR Testing

SSR tests were performed in the same autoclaves that were used for the FT testing. The button head SSR samples were installed on clevises inside the autoclaves, then the same autoclave charging procedure described in section 4.1.2 was followed to achieve oxygen levels lower than 1 ppm and moisture level less than 10 ppm in the autoclave prior to starting SSR testing. SSR tests were performed using servo electric frames which record the load and displacement of the testing samples. All samples were strained until failure. The SSR testing parameters are summarized below:

- Strain rate: 1.25×10^{-5} 1/s

3.2.1 Specimen Examination

Upon completing the SSR tests, all specimens were removed from the test vessel and the diameter of the sample near the fracture location was measured using a stereomicroscope. This value was used to calculate the reduction in area (RA). The samples were also examined to document any indication of brittle failure or secondary cracking.

3.3 Hydrogen Flux Measurement

Hydrogen flux measurement was performed using the Devanathan-Stachurski cell technique and the instructions described in ASTM G148 /4/. The experimental setup is shown in Figure 7. The experimental setup consists of a C276 autoclave on the hydrogen charging side and an acrylic cell on the oxidation side. A disk sample with 3 mm thickness was used in hydrogen flux test, as shown in Figure 8.

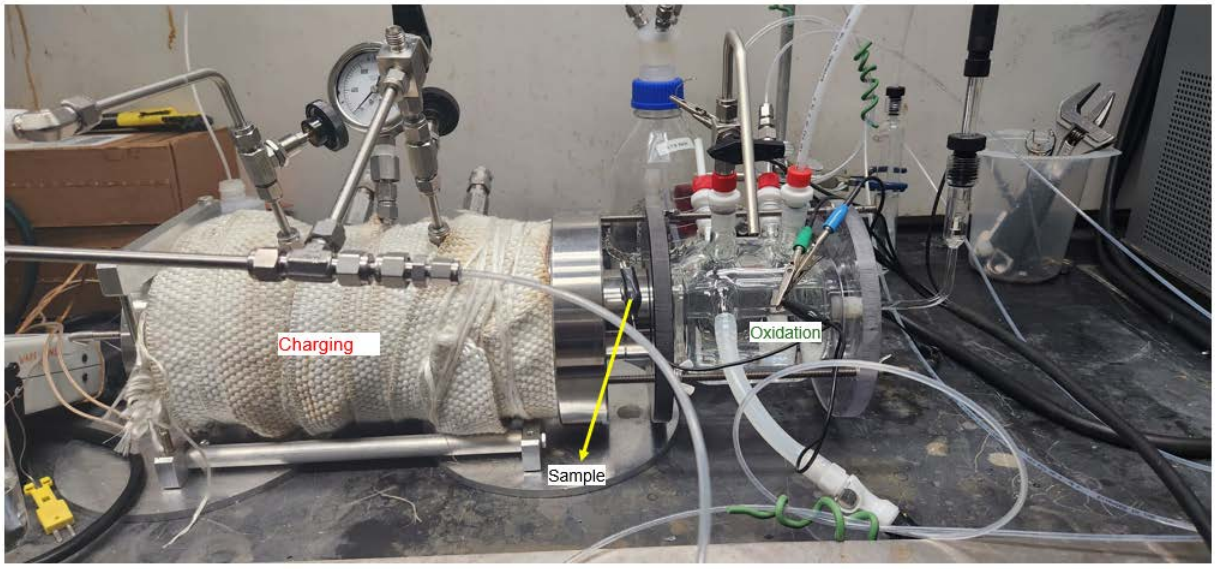

Figure 7. Hydrogen flux experimental setup

The oxidation cell contains 0.1 M NaOH solution that is constantly purged using high purity nitrogen. A Pt/Nb wire loop and a saturated calomel electrode (SCE), were used as counter and SCE reference electrodes, respectively.

Prior to starting test, the NaOH solution and the oxidation cell were both deaerated with high purity nitrogen overnight. Once the solution and the cell were fully deaerated, the solution was transferred to the oxidation cell under nitrogen pressure to avoid any oxygen ingress into the oxidation cell. The sample then was polarized to 0.3 V vs. SCE while the current was measured to establish a steady background. Typically, a background current density lower than 100 nA/cm^2 is expected. After the background current density fell below 100 nA/cm^2, the autoclave was subjected to the same charging procedure as that used in the FT testing and SSR testing. This provided low oxygen and moisture conditions on the charging side and to establish 100 bara hydrogen pressure to begin hydrogen flux measurement. Constant applied potential on the oxidation side would facilitate oxidation of any hydrogen diffusing through the sample from the charging side. When hydrogen diffuses through the testing sample, this would result in a current transient, i.e., current increasing and then reaching a plateau, that could be used to convert to diffusion flux and calculate the hydrogen diffusion coefficient.

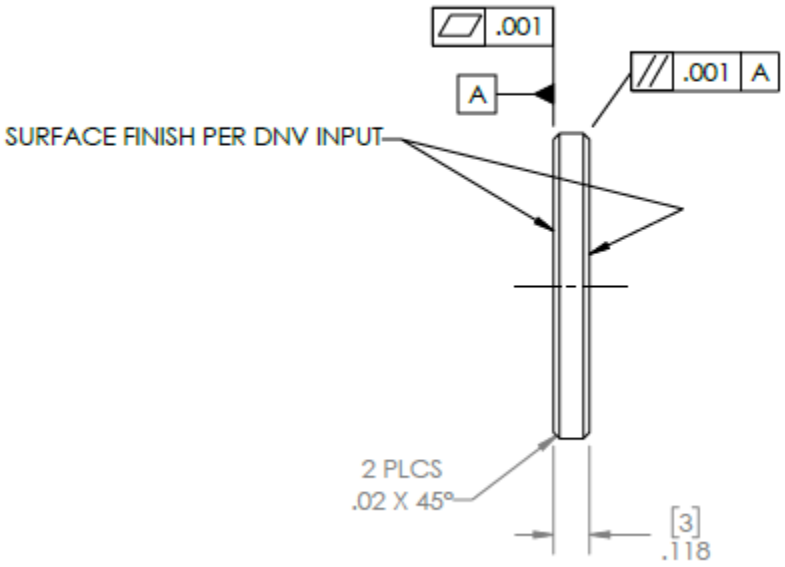

Figure 8. Dimensions of the hydrogen flux sample.

4 Data Analysis

4.1 FT Data Analysis

The data from the FT tests was analyzed using ASTM E1820 /2/. The fracture toughness J was calculated from the sum of the elastic and plastic components according to equations (1) to (3) below:

$$J_{tot} = J_{el} + J_{pl} \tag{1}$$

$$J_{tot} = \frac{K_{(i)}{}^{2}(1-\upsilon^{2})}{E} + J_{pl(i)} \tag{2}$$

$$J_{pl(i)} = \left[J_{pl(i-1)} + \left(\frac{\eta_{pl(i-1)}}{b_{(i-1)}}\right)\frac{A_{pl(i)} - A_{pl(i-1)}}{B_N}\right]\left[1 - \gamma_{(i-1)}\left(\frac{a_{(i)} - a_{(i-1)}}{b_{i-1}}\right)\right] \tag{3}$$

where:

i: step

K : Stress Intensity Factor (N·mm$^{-3/2}$)

$$K = \frac{P}{(BB_N W)^{1/2}} f(\frac{a}{W})$$

P: load (N)

υ : Poisson's Ratio, 0.32

E : Young's Modulus (MPa): assumed to be 200138 MPa (29000 ksi)

$\eta_{pl(i-1)} = 2 + 0.522 b_{(i-1)} / W$

$\gamma_{pl(i-1)} = 1 + 0.76 b_{(i-1)} / W$

A_{pl} : Plastic component of the area under the Load CMOD curve (based on ASTM E1820 A2.4.2.2, equations A2.9, A2.10 and A2.11)

B : Sample thickness (mm)

B_N: Sample thickness at the root of side grooves (mm)

W : Sample width (mm)

a : Crack length (mm)

b : Remaining ligament (mm), *W-a*

The processed J vs. ∆a was fitted to equation (4) below:

$$J=A_J \Delta a^{\beta} \quad (4)$$

The fitting parameters, J at 0 mm (point of first crack extension), 0.2 mm and 1 mm of crack extension and the J value at the maximum load are reported. **The value $J_{maxload}$** is the derived at the maximum force. These J values were also converted to K_J using equation (5) below:

$$K_J = \sqrt{\frac{JE}{1-\nu^2}} \quad (5)$$

4.2 SSR Data Analysis

SSR data was analyzed to determine the plastic elongation (E_p) in accordance with the instructions in NACE TM0198 /5/.

4.3 Hydrogen Flux Data Analysis

In the case hydrogen diffusion does occur, and hydrogen oxidation current is measured, the rising transient of the sample can be expressed by the following equation:

$$\frac{i_t - i_0}{i_\infty - i_0} = \frac{2L}{\sqrt{\pi D t}} \sum_{n=0}^{\infty} \exp\left(-\frac{(2n+1)^2 L^2}{4Dt}\right) \qquad (6)$$

Where: i_t – transient current at time t (A/cm^2)

i_0 – initial current at t=0 (A/cm^2)

i_∞ – steady state current at t→∞

L – sample thickness (cm)

t – time (s)

D – diffusion coefficient (cm^2/s)

A Matlab script was used to do a regression and generate flux data and calculate the diffusion coefficient.

Appendix B: Experimental Details for API Material Testing in Hydrogen from Test Lab B

1 MATERIALS AND SPECIMEN GEOMETRIES

Two materials were provided for evaluation: low-alloy steel 4140 in the 110 ksi temper and 718 in the 120 ksi condition (API 6ACRA UNS N07718-125). Material certifications from the manufacturers are provided in Appendix A. The materials were nominally 5 inches in diameter and sufficient quantifies were provided to fabricate all necessary specimens and spares. The material forms and nominal tensile properties as provided in the material test reports are provided in Table 1.

Table 5. Material forms and tensile properties from material testing reports provided by API.

Material	Form	0.2% Yield Stress (ksi)	Ultimate Tensile Stress (ksi)	Elongation (%)	Reduction of Area (%)
4140	5-inch round	142.1	157.9	18.9	57.9
Alloy 718	5-inch round	135.2	181.8	27.6	40.2

All test specimens were excised at the mid-radius as shown in Figure 1. The fracture toughness specimens were oriented in the C-L orientation, and the tensile bars were fabricated in the L orientation. A cut plan was developed for each material and provided to API for review prior to specimen fabrication (see Figure 2). Test specimens were fabricated as outlined in ASTM E1820 for the fracture toughness testing and E8 for the tensile testing (see Figure 3 through Figure 5). Two different compact tension (CT) specimen geometries were utilized for the toughness testing, with the air specimens being larger due to a higher anticipated fracture toughness in the absence of hydrogen (width (W) equal to 2 inches and thickness (B) equal to 1 inch). This larger specimen ensured valid test results and J-dominance. The hydrogen test specimens were fabricated to be compatible with existing autoclave hardware (W of 1.25 inches and B of 0.30 inches). After fatigue precracking, the specimens were side-grooved nominally 20% total in the thickness dimension (10% on each side).

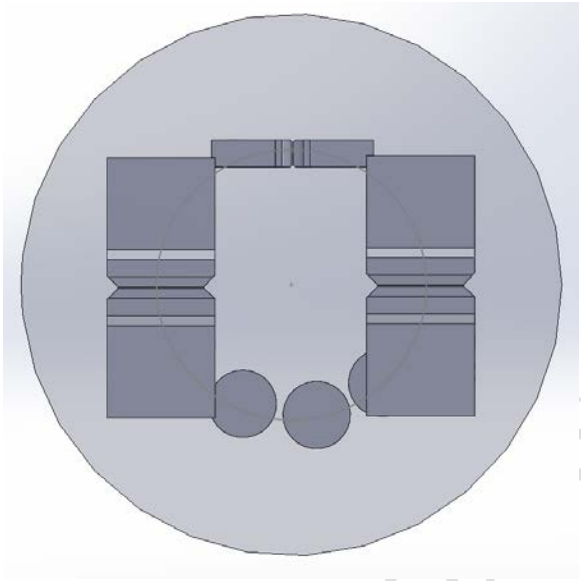

Figure 9. Test specimens were excised at the mid-radius of the provided round stock.

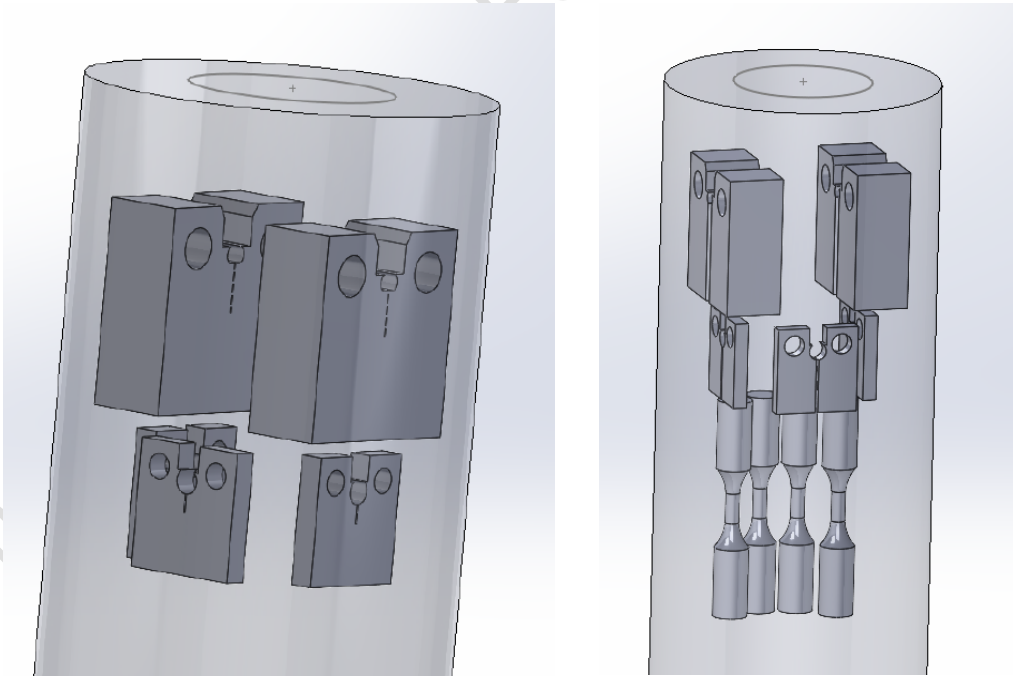

Figure 10. Cut plans for 4140 (left) and 718 (right). The circle on the top surface of each round shows the mid-radius locations.

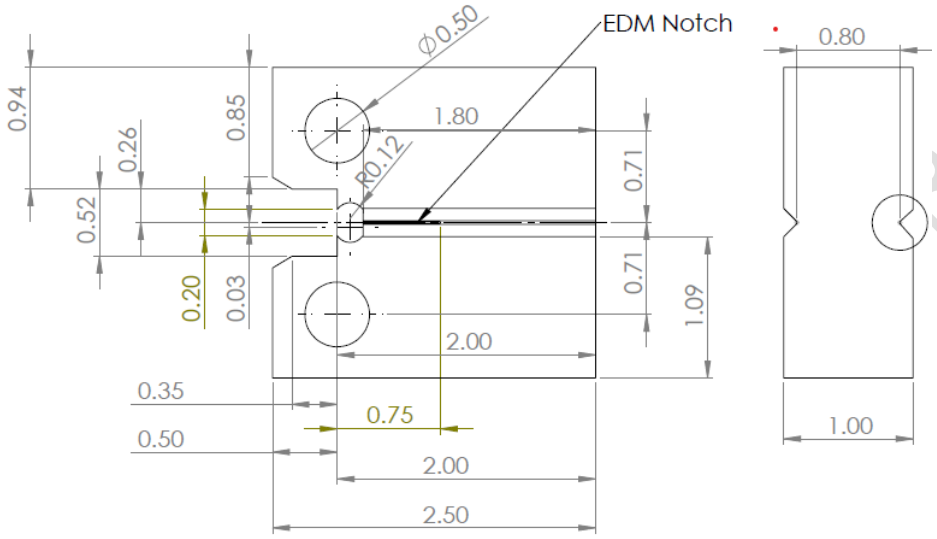

Figure 11. Compact tension specimen geometry for baseline fracture toughness tests with width of 2.0 inches and thickness of 1.0 inch in keeping with ASTM E1820.

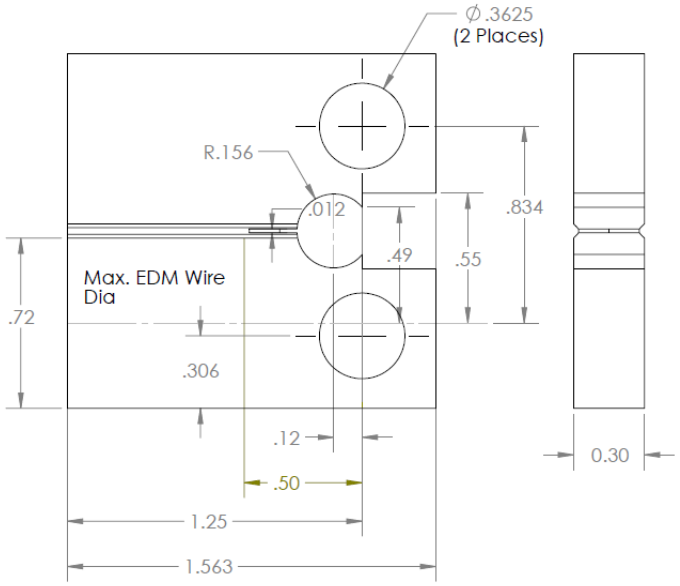

Figure 12. Compact tension specimen geometry for fracture toughness tests in hydrogen gas with width of 1.25 inches and thickness of 0.3 inches in keeping with ASTM E1820.

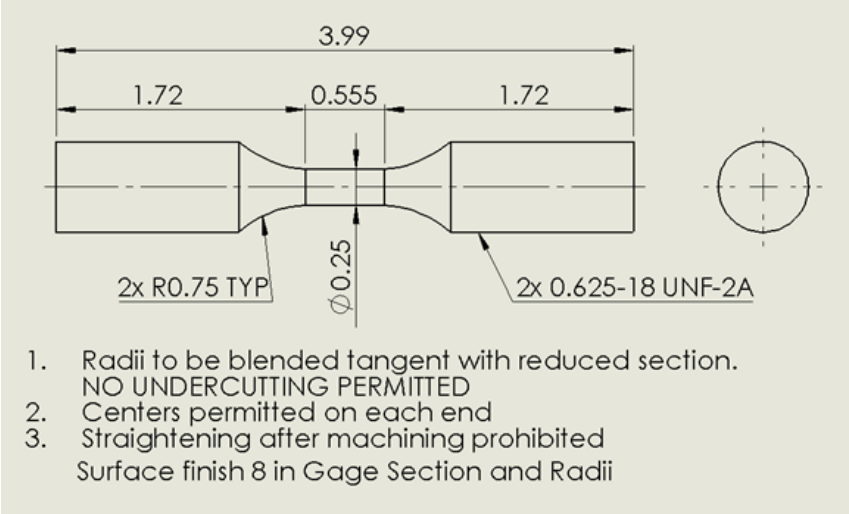

Figure 13. Tensile test specimen geometry in keeping with ASTM E8.

2 TEST METHODS

In this testing program, fracture toughness and tensile tests were performed. The fracture toughness testing was completed in air and 100-bar hydrogen gas on two materials: low-alloy steel 4140 and alloy 718. The tensile testing was performed on the 718 only in 100-bar hydrogen and 100-bar helium, and the permeation testing was completed on the 718. High-purity hydrogen gas (99.999%) was utilized for all hydrogen testing. The following sections describe the test methods for the identified tests.

a. Fracture Toughness

The objective of this task was to apply the test method E1820 to measure the crack initiation toughness (J or K_J) and cracking resistance curves (J-R curves) of each material in air and 100-bar hydrogen gas. Test specimens were fabricated per the cut plan and specimen drawings and then fatigue precracked in lab air. After precracking, specimens were sidegrooved to nominally 20% (10% each side). For the hydrogen gas tests, specimens were not precharged or presoaked, and testing was started as soon

as steady-state conditions (temperature and pressure) were achieved in the autoclave. The crack initiation toughness and cracking resistance curves were measured on duplicate specimens for each material in 100-bar hydrogen gas. In addition to these hydrogen gas tests, test method E1820 was performed on at least one specimen for each material in lab ambient conditions to determine the baseline crack initiation toughness and J-R behavior.

The elastic-plastic fracture mechanics methods in ASTM E1820 were utilized to measure fracture initiation toughness and crack growth resistance. The anticipated fracture toughness values (J_{IC}) from the technical literature were used with the yield stress of each material to determine the minimum specimen thickness (B) and remaining ligament length determined by the specimen width and crack length (a) to ensure J-dominance and valid toughness results.

$$W - a, B > 10\, J_Q / \sigma_Y$$

Integral knife edges were fabricated into the specimens to measure the load-line crack opening displacement (COD) throughout each test. Integral knife edges allowed secure attachment of COD or clip gages to the test specimens. Following fabrication, the specimens were polished in and around the crack extension zone, and a lab data sheet was created to document test specimen dimensions and subsequent test steps. After precracking and sidegrooving, the hydrogen gas tests were instrumented with direct current potential drop (DCPD) probes to measure the in-situ crack extension.

The hydrogen gas tests were performed in autoclaves coupled to servohydraulic test frames. The test specimens were placed into the load train, and the DCPD wires were fed through ports in the autoclave head. The COD gage was attached, and DCPD probes were connected to the test system. The system was sealed, leak-checked using high-pressure nitrogen gas, and then purged using SwRI standard operating procedures. To ensure gas purity in the test autoclave, the autoclave was placed under vacuum, and a series of nitrogen gas and hydrogen gas purges were performed. The autoclave was then pressurized with high-purity hydrogen gas to the prescribed testing pressure. These procedures have been verified with gas sampling to achieve less than 1 ppm O_2 and less than 5 ppm H_2O. As prescribed in ASTM E1820, tests were performed under actuator displacement control at a constant rate. The displacement rate was calculated based on specimen dimensions and compliance to achieve a target initial K-rate of 1 MPa$\sqrt{m}$ per hour (or 0.91 ksi$\sqrt{in}$. per hour).

For the air tests, the unloading compliance method was utilized to infer crack length from the specimen compliance by periodically unloading the specimens during the tests, and for the hydrogen gas tests, the crack length was measured using direct current potential drop (DCPD) as outlined in ASTM E1820 Annex 18 and periodic unloads were not used to infer crack length. The air tests were controlled and post-test analyzed using Fracture Technology Associates (FTA) software and hardware. This software automates the periodic unloading segments and accurately controls the test. The FTA software has an integrated software package for post-test analysis to develop J-R curves, identify the cracking initiation toughness (J_Q), and determine if validity requirements were satisfied.

For the hydrogen gas tests, load, crack-opening displacement, and DCPD voltage (converted to crack length) were continuously measured throughout each test using a LabVIEW-based data acquisition system. Based on these data, the J versus crack extension (Δa) curves were constructed using a MATLAB script following procedures specified in ASTM E1820. The crack length was calculated per a linear transformation from DCPD voltage and not as outlined in Annex 18 of the standard. From this construction, the crack initiation toughness (J_Q) was identified, and all validity criteria were evaluated.

b. Slow Strain Rate Testing

Tensile testing in 100-bar helium (inert) and 100-bar hydrogen gas environments was performed in accordance with ASTM G142. This testing utilized a servohydraulic test frame outfitted with an autoclave for high-pressure high-temperature hydrogen gas testing. Tests were controlled at a constant actuator displacement rate to achieve a target strain rate of $1e^{-5}$ per second, and test data were collected from each test with a LabVIEW-based data acquisition system. The gage section displacement was measured in-situ using an extensometer, and strain was calculated from this local displacement measurement. For each test, the load, pressure, extensometer, and actuator LVDT displacement were continuously collected. The autoclave preparation followed standard SwRI procedures for ensuring gas quality as previously described.

Stress-strain curves were developed for each test, and the following tensile test parameters were determined: 0.2% yield stress, the ultimate tensile stress, the elongation (EL), and the reduction in area (RA). The elongation was determined from gage marks scribed on the specimen before testing, and after testing this distance was measured using a traveling microscope and compared to the initial distance. The reduction of area was calculated from the minimum diameter of each specimen after testing and the specimen diameter before testing. The inert (helium) test data were compared to the gaseous hydrogen data, and the HEE indices for elongation and reduction of area were calculated as outlined in Lee (2016) per the following:

HEE Index RA = RA in Hydrogen/RA in Inert *100%

HEE Index EL = EL in Hydrogen/EL in Inert*100%

c. Hydrogen Permeation Testing

A permeation membrane was machined from the Alloy 718 bar material. The sample was removed from the midwall facing the OD of the bar. The rectangular membrane had dimensions of 1.55 inches width, 1.76 inches length, and was 0.118 inches (3 mm) in thickness as seen in Figure 1. The one side that would

be exposed to the oxidation cell (detection side) was coated with Pd prior to testing. The dimensions of the membrane were measured and recorded.

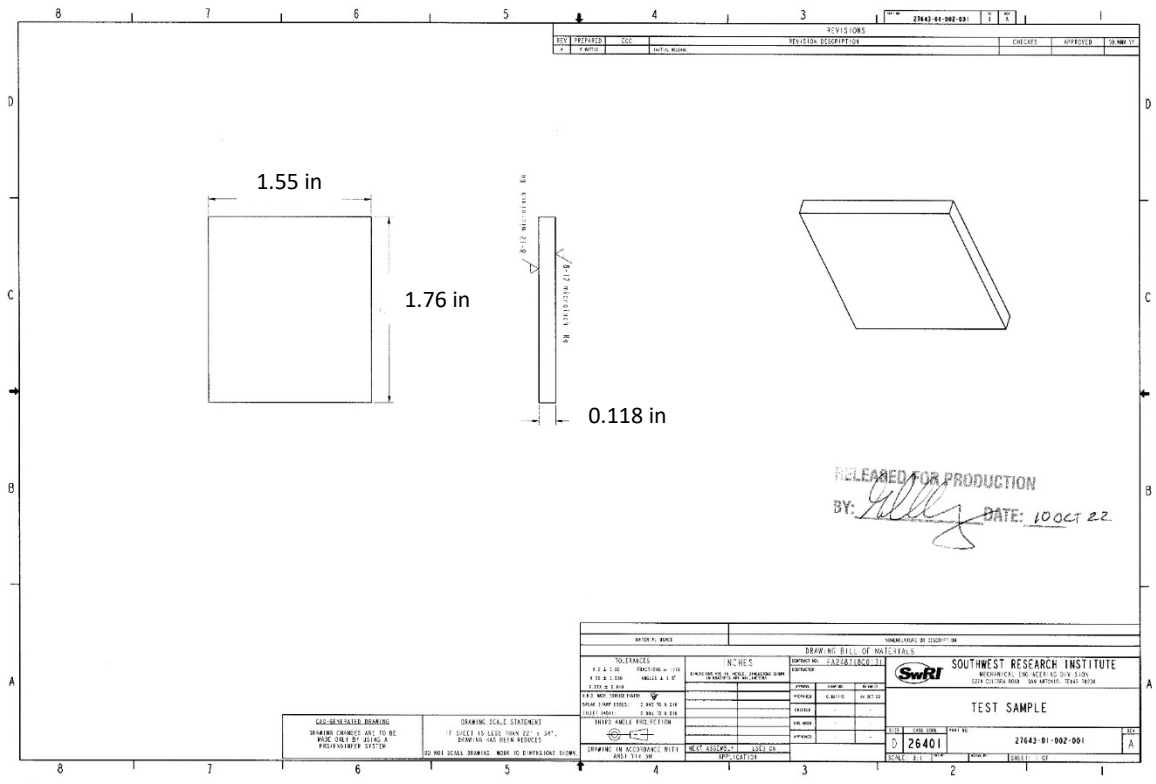

Figure 14. Drawing of Hydrogen Permeation Membrane.

3 TEST METHOD

Hydrogen Permeation Testing at High Pressure – Hydrogen permeation testing was performed in a specialized stainless steel high pressure autoclave test apparatus. Testing was performed using an electrochemical technique per ASTM G148 - Standard Practice for Evaluation of Hydrogen Uptake, Permeation, and Transport in Metals by an Electrochemical Technique. This assembly, which is shown in Figure 2, has two chambers: a charging side with the high pressure gaseous environment and an oxidation side where the hydrogen permeating through the sample is measured. The holder was fabricated to adjust the

exposed area considering the strength of the material, thickness of the membrane and test pressure. The machined and Pd coated membrane was placed in the holder in between two stainless steel plates. A seal is created by tightening the plates between the flanged ends. The charging side was then thoroughly deaerated and pressure checked prior to testing using 100% helium gas.

Figure 15. Photograph of high pressure permeation apparatus. The charging side has the high pressure gaseous environment and the oxidation side has the electrochemical environment to measure the hydrogen permeating through the sample.

A 0.1M NaOH solution was prepared separately and deaerated overnight using high purity Nitrogen gas. The solution was then transferred into the oxidation side of the test apparatus using the high purity Nitrogen gas to avoid oxygen inclusion. A platinum mesh was used as the counter electrode and a Ag/AgCl electrode

was used as the reference electrode. A +100 mV vs. SCE potential was applied on the sample and a background current was obtained in the nA range. It is beneficial to obtain a nA range background current in order to observe the current transient rise.

Once the background current was reached, a 100 bar (1,450 psi) H_2 gas was introduced into the charging side of the permeation cell at ambient temperature. During permeation testing, hydrogen diffuses through the membrane and becomes oxidized (on the oxidation side of the cell) and current is measured using a potentiostat. A current transient rise is then observed and over time reaches a steady state (hydrogen permeation current). Measurements are recorded until a steady state current was obtained. The steady state hydrogen flux (J_{ss}) is obtained through the relationship:

$$\mathbf{J_{ss} = I / A*F}$$

where

I - steady state permeation current, Amp

A - area, cm^2

F - Faradays constant, C/mol